Chapter III

Liquid Crystal Based Temperature And Heat Transfer Measurements Using A Transient Method

Test Case : Impinging Round Jet

Cengiz Camci

The Pennsylvania State University
Department of Aerospace Engineering

Summary

A transient heat transfer method using the color recognition idea (hue capturing) described in Chapter II is presented in this chapter.. In order to explain the use of hue-capturing

technique as a laboratory class heat transfer measuring tool, the heat transfer characteristics of impinging jets are investigated. The heat transfer coefficients are also measured by fast response thin foil thermocouples for comparison with the hue-capturing technique results. Mean velocities and turbulent intensities of the jet flow field are measured by using a five-hole probe and a single sensor hot-wire for a better understanding of flow physics during the validation of the suggested hue-capturing technique. Extensive results from a combined fluid mechanics and heat transfer study using transient liquid crystal thermography are provided.

List of Symbols

c	=	specific heat
CCD	=	charge coupled device
C_f	=	skin friction coefficient , $C_f = \tau_w/(0.5\rho U_b^2)$
C_p	=	pressure coefficient
D	=	jet nozzle diameter
H	=	distance between nozzle exit and the impingement plate
h	=	convective heat transfer coefficient, $h=q/(T_w-T_{rec})$
h'	=	convective heat transfer coefficient, $h'=q/(T_w-T_{jmax})$
HSI	=	normalized hue, saturation, intensity
k	=	thermal conductivity
l_n	=	jet nozzle length
n	=	normal distance from the wall surface
NTSC	=	National Television System Committee
Nu	=	Nusselt number $Nu=hD/k$
Nu'	=	Nusselt number $Nu'=h'D/k$
p	=	pressure (N/m^2)
q	=	heat flux
r	=	radial coordinate
Re	=	Reynolds number
RGB	=	normalized red , green and blue
R35C1W	=	Chiral Nematic Liquid Crystal starting to respond at about 35 ^{0} C
with		an approximate bandwidth of 1^0 C
T	=	temperature
t	=	time
Tu	=	turbulence intensity, $Tu=u/U$
U	=	mean velocity
u	=	rms value of fluctuating velocity
x,y	=	cartesian coordinates or pixel coordinates

Greek Symbols

α	=	thermal diffusivity of air
β	=	non-dimensional time
ρ	=	density
τ	=	shear stress

| θ | = | non-dimensional temperature |

Subscripts

a	=	ambient condition
b	=	bulk mean
f	=	fluid
i	=	initial condition
j	=	jet exit condition
max	=	maximum value
p	=	at constant pressure
r	=	radial component
rec	=	recovery condition
ref	=	reference value
static	=	static condition
total	=	total condition
w	=	wall condition

III . 1 Experimental Apparatus and Technique

III.1.1 _Flow System_ : The flow system consists of a centrifugal blower, a settling chamber, a heater, a pipe nozzle and an impingement plate. Figure 3.1 shows the schematic of the flow system and the definition of coordinates of the jet flow field. A blower with a continuously adjustable electric motor supplies air to the settling chamber. The settling chamber reduces the inherent pressure fluctuations of the air from the blower. The air is heated to the desired temperature in the electrical heater section. Then it passes through the nozzle and finally impinges onto the target plate.

The heater section contains a horizontal heater element situated along the centerline of a circular pipe having a 5.08 cm diameter. The heater consists of Nichrome-60 wire of 22 gauge that is wrapped around a Molite refractory ceramic rod of 1.2 cm diameter and 35 cm length. Three screens are employed at the end of heater section to provide a smooth temperature profile. The nozzle section is a PVC pipe of 3.81 cm internal diameter, with a square cut exit section. The length of the pipe is 91.44 cm, resulting in a length to diameter ratio of 24. The distance H between the nozzle exit section and the impingement plate is adjustable.

III.1.2 _Five-hole Probe and Hot Wire Measurements_ : A subminiature five-hole probe was employed to obtain the distributions of three orthogonal velocity components, stagnation

pressure and static pressure. Figure 3.2 describes the geometric details of the probe and the definitions of calibration coefficients. The diamond shaped probe tip had an overall diameter of 1.68 mm and consisted of four holes set 45 degrees off the reference line and the fifth center hole. These five holes provided five pressures to a 48J9-1 Scanivalve system, a pressure sampling scanner. The output of the scanner was measured with a ± 0.2 psi range Validyne DP-15 variable reluctance pressure transducer. The measured pressures were relative to atmospheric pressure. A precision U tube manometer was used for the calibration of the pressure transducer. The estimated time response of the transducer was about 1 KHz.

The five-hole probe was calibrated in the Hot-Air Wind Tunnel Facility located in The Turbomachinery Laboratory of The Pennsylvania State University. The calibration was performed in both yaw and pitch planes with an interval of 10 degrees ranging from -30 to 30 degrees. The calibration results obtained in a flow velocity of 30 m/sec are shown figure 3.3. Details of the calibration methods were described by Treaster and Yocum (1979). They showed that the Reynolds number effect is reasonably small, for the specific probe and the data reduction method.

Local total and static pressure, pitch and yaw angle, and the three orthogonal velocity components can be computed from the measured pressure data using the calibration curves. Various pressure coefficients are calculated from the five pressure data. A bi-linear interpolation procedure on the first calibration chart (figure 3.3a) gives the values of α and β. The values of Cp_{static} and Cp_{total} are then calculated from figure 3.3b and 3.3c, respectively, again using a bi-linear interpolation procedure. Local total and static pressures are then calculated and are used in Bernoulli's equation to find the magnitude of the local velocity as:

$$ (3.1) $$

Finally three orthogonal velocity components are computed from the defined vector relationships shown in figure 3.2.

The turbulent intensity and mean velocity of the jet flow field were acquired with a single sensor hot-wire probe. The hot-wire probe was manufactured by Dantec (type 55p13). The sensor was made of 5 μm tungsten wire with length-to-diameter ratio of approximately 300. The probe resistance was 3.49 Ω at 20 ^{0} C . An AN-1003 hot-wire/hot film anemometer system manufactured by A. A. Lab Systems was used to operate the hot-wire at constant temperature. The operating resistance was set at 1.7 times the measured cold resistance. The hot-wire probe was calibrated for the velocities up to 30 m/sec. Figure 3.4 shows the typical calibration results of anemometer output versus velocity. A fourth order polynomial response function to be used in the real measurements was obtained from the calibration data.

III.1.3   Transient Heat Transfer Measurements on the Impingement Plate : Forced convection heat transfer from a heated jet to an impingement plate depends on the temperature rise of the model surface when   subjected to a transient convective heating or cooling. The transient technique, reviewed by Schultz and Jones (1973) uses the timewise variation of wall temperature as a measure of the wall heat flux q_w and the corresponding heat transfer coefficient (h). When the model has a low thermal conductivity (k), the wall   temperature response is limited to a thin layer near the wall surface and the lateral conduction is very small. Therefore the heat conduction into the model may be assumed to be one dimensional into a semi-infinite medium. Saabas et al. (1987) showed the validity of the one-dimensional heat flow assumption.

Transient heat transfer into a semi-infinite medium with constant thermal properties is governed by the transient one-dimensional diffusion equation

$$(3.2)$$

where α is thermal diffusivity.

The boundary and initial conditions can be stated as follows:

at n=0 (3.3)

at   n = -∞ (3.4)

at   t = 0 (3.5)

where $(T_w\text{-}T_{ref})$ and T_i are wall surface temperature at time t , reference temperature (usually constant free stream fluid temperature) and initial wall surface temperature, respectively.

The solution of the above equation system relates the wall surface temperature history to heat flux:

$$(3.6)$$

In this form there is, however, a singularity in the integral term at $t=\tau$ which will give rise to error in heat flux computation. This error will in general be larger for small t . Numerical integration of the second part of the expression moves the singularity out of the denominator. Jones (1959) recommended a trapezoidal rule to evaluate the integral over the first (n-1) time divisions and a linear temperature-time relation for the last interval.

$$(3.7)$$

This equation integrates the measured temperature history to give heat transfer coefficients.

The temperature histories were measured experimentally with thin foil K-type thermocouples in this study. An interesting feature of equation 3.7 is that , the reconstruction of any heat flux transient is possible with all the conditions defined in equations 3.3, 3.4 and 3.5. The model can handle strong transients in wall temperature or wall heat flux in time. However the overall solution is time consuming because it requires the knowledge of complete time history of wall temperature from the start of a transient experiment.

Another approach for the measurements of heat transfer coefficient requires additional assumptions. First, the heat transfer coefficient is assumed constant in time. And if a step change in the fluid temperature is induced, equation (3.2) can be solved to give the surface temperature as

$$(3.8)$$

where β is non-dimensional time defined as:

$$(3.9)$$

Then, a single measurement of surface temperature at a certain time enables the heat transfer coefficient to be found when the reference temperature, initial temperature and the thermal properties are known. If the convective heat transfer coefficient is known to be constant in a transient experiment , then equation 3.7 and equation 3.8 are supposed to generate identical solutions in terms of convective heat transfer coefficient h. One should pay attention that equation 3.7 requires the knowledge and processing of complete wall temperature history from the beginning of the transient experiment. However, equation 3.8 is based on a single point processing of wall temperature data which is more easy to implement into a liquid crystal thermography based method. Equation 3.7 provides the basic equation of the specific heat transfer coefficient measurement technique using the images captured on liquid crystal covered surfaces. In this approach, any spatial variation in heat transfer coefficient will generate a corresponding variation in surface temperature which varies during a transient experiment. This spatial variation of surface temperature does not cause the heat transfer coefficient to vary in time significantly as discussed by Ireland and Jones (1985).

In the present experiments, the impingement plate material chosen was acrylic which has

low thermal conductivity. A thermophysical triple product $(\rho c k)^{0.5}$ of 569 W(sec)$^{0.5}$/(m^{2}K) was used in the data reduction with the uncertainty band of 5 % as reported by Baughn et al. (1986). Initially the plate temperature was kept constant at room temperature and the heated jet was diverted by a flow diverter consisting of a removable 90 degree elbow section. The flow diverter was used to guarantee no influence of the heated jet on the uniform initial temperature distribution of the impingement plate. With the remove the flow diverter, the heated jet suddenly impinged on the plate. The room temperature and the jet maximum temperature was kept near 23 ^{0}C, and 50-60 ^{0}C, respectively. A liquid crystal layer coated on the model surface was used to monitor the surface temperature. Details of the calibration of the liquid crystals and associated uncertainties are given in Chapter II. As the model surface temperature changed, a band of color moved across the surface. If the model were initially isothermal, the band of constant color would represent a line of constant heat transfer coefficient. Then the measurements of required times to reach the known color display temperature would allow the solution of equation (3.8) for the heat transfer coefficients. A polynomial curve fitting routine was developed for the variation of the non-dimensional time β with respect to the non-dimensional wall temperature θ from equation 3.8. The final form of a sixth order representation used in reducing the liquid crystal image data is as follows;

(3.10)

III.1.4 ***Data Acquisition and Probe Traversing System*** : A Metrabyte DASH-16 high speed analog/digital I/O expansion board was employed to acquire data from the five-hole probe, hot-wire, and thermocouple. It enabled the simultaneous acquisition of data from up to 16 different channels which were connected to different probes. All data were fed into an AT&T 6300 computer where they were processed. The binary ouput of DASH-16 board was used to control the scanivalve system. Four other digital outputs were responsible for operating two stepping motors. One stepping motor traversed horizontally and the second one vertically, holding the probe.

III . 2   Flow Field Surveys and Discussion

This section describes the experimental results of the flow field characteristics of a heated axisymmetric round jet impinging on a normal plate. The mean velocities and turbulent

intensities were measured using a five-hole probe and a single sensor hot-wire. The measurements were performed for three Reynolds numbers, Re=30,000, 40,000 and 50,000. Another measurement parameter was the ratio of the distance from the nozzle exit to the impingement plate (H) to the nozzle exit diameter (D). The measurements were carried out for H/D=2, 4, 6 and 8. The effect of the variation in these parameters has been characterized.

Figure 3.5 shows the velocity vector distributions measured with the five-hole probe for Re=30,000 and H/D=8. In this figure, the flow pattern can be subdivided into three characteristic regions: the free jet region, the stagnation flow region, and the wall jet region. Immediately on leaving the nozzle, the air in the jet starts to entrain the surrounding still air. By an intensive exchange of momentum, the jet spreads continuously up to a limiting distance where the mixing region is wide enough to penetrate to the centerline of the jet. The velocity profiles within the potential core like region are relatively unaffected by mixing and are similar to the nozzle exit velocity profile. Beyond the potential core like region the jet decays rapidly as the jet shares its momentum with more and more entrained fluid. In the stagnation flow region, the flow changes its direction due to a strong adverse pressure gradient. Beyond the point at which the strong interactions of impingement cause any local effects, the radial wall jet flow develops along the surface. For H/D=4, as shown in figure 3.6, the flow stagnates onto the plate before the potential core like region disappears. No significant change in the velocities non-dimensionalized by the bulk mean velocity due to Reynolds number variation is observed in figures 3.6 and 3.7. The jet exit mean velocities measured at the nozzle edge radius show directional error due to strong velocity gradients as shown in figures 3.5, 3.6 and 3.7. The main portion of the measurement error is due to the fact that the diameter of the five-hole probe is larger than the shear layer thickness in this extremely narrow region.

Mean velocities and turbulent intensities are measured by a single sensor hot-wire at the nozzle exit as shown in figure 3.8 and 3.9. The results are plotted as a function of radial distance measured from the jet centerline normalized by the nozzle diameter. The shape of the mean velocity and turbulent intensity distributions at the nozzle exit are independent of both Reynolds number and the distance from the nozzle exit to the plate. The mean velocities show a maximum at the jet centerline and decrease monotonically in the radial direction. The peak values of the turbulent intensity correspond to the nozzle edges, whereas the relative minimum values are related to the jet centerline.

Figure 3.10 shows the axial decay of the centerline mean velocity and the variation of the centerline turbulent intensity for Re=30,000. When the impingement plate is removed, the centerline mean velocity remains nearly constant ($U/U_b \approx 1.25$) in the potential core like region. The potential core like region is thought to extend to about five nozzle diameters downstream of the nozzle exit. Most prior studies show a potential core like region of five to six nozzle diameters long which is consistent with the present study. The mean velocity suddenly decreases when the mixing layers merge into the centerline beyond the potential core like region; while, the turbulent intensity of the free jet shows a sharp increase at the end of the potential core like region. With the impingement plate in place, the mean velocity and turbulent profiles follow

well those of the free jet without the plate except in the stagnation flow region. In the stagnation region, the mean velocity suddenly drops to zero, while the turbulent intensity shows a significant increase before it drops to zero.

The radial distributions of the mean velocity and turbulent intensity in the free jet region for Re=30,000, and H/D=8 are shown in figure 3.11. Five-hole probe and single sensor hot-wire results agree very well and both characterize the jet spread and decay in figure 3.11a. Initially, the turbulent intensity peak appears in the center of the mixing region, i.e., at the nozzle radius r/D=0.5. This peak is increased dramatically in the early stage of the mixing. However, the centerline turbulent intensity starts to show a significant increase only at the end of the potential core like region. The turbulent intensity levels at the nozzle edge radius are much larger than those of the centerline for x/D=2 and 4. Beyond the potential core like region, the turbulent intensity peak located initially at the nozzle radius gradually moves toward the centerline. The turbulent intensity profile is much smoother for x/D=6 due to the increase of the centerline turbulent intensity. The flow stagnating onto the impingement plate is mixed and highly turbulent. Figure 3.12 and 3.13 show the mean velocity and turbulent intensity profiles for Re=30,000, and 40,000, respectively. The distance between the nozzle exit and the impingement plate, H/D was 4 for both cases. These figures indicate that both non-dimensional mean velocity and turbulent intensity profiles are not affected by Reynolds number, in this specific range. For H/D=4, the potential core like flow of relatively low turbulent intensity stagnates onto the impingement plate.

The total mean velocity distributions in the near wall region are in figure 3.14. The agreement between the five-hole probe and single sensor hot-wire measurements are very good. Since the velocity is zero at the stagnation point, the wall boundary layer grows fast immediately after that point. The mean velocities in the wall layer show maxima around r/D=1, then decrease due to diffusion. The wall boundary layer and free jet layer grow together, forming a typical wall jet profile.

In the vicinity of the wall, the five-hole probe introduces wall-proximity errors. Considering the agreement with the hot-wire results, this error seems to be negligible in the present measurement range. It should be noted in figure 3.14 that the first five-hole probe measurement location is the third measurement position for the corresponding hot-wire measurements. The wire diameter is of the order of 5 μm. Figure 3.15a shows the turbulent intensity distribution in the near wall region for Re=30,000 and H/D=8. Turbulent intensity in the near wall region shows maximum in the stagnation region and monotonically decreases along radial direction. In this case, the fully mixed free jet provides the maximum turbulent intensity at jet centerline before stagnation and the flow of the maximum turbulent intensity hit the stagnation point of the plate. Figure 3.15b and 3.15c, which are for H/D=4, show quite different characteristics. Turbulent intensity peak appears around r/D=2 radial location with the impingement plate at H/D=4 for both Re=30,000 and 40,000. It has been conjectured that the mixing core region flow of the peak turbulent intensity rapidly diverges close to the impingement plate and meets the plate around r/D=2; while, the potential core like flow of low turbulent intensity meets the plate in the stagnation

region, resulting in relative minimum turbulent intensity in that region.

III . 3   Heat Transfer Results and Discussion

A very powerful application of the hue-capturing technique is the   generation of convective heat transfer coefficients from color images.   In this study, the convective heat transfer characteristics of impinging jets are investigated by using the hue-capturing technique based on the   transient heat transfer technique described in section 3.1.5. The heat transfer coefficients are also obtained by fast response   thermocouple temperature history measurements for comparison.

The convective heat transfer coefficient is defined as the wall heat flux divided by the difference between the surface temperature and some characteristic temperature of the fluid. Usually the jet maximum temperature is used as the characteristic fluid temperature since it is convenient to obtain. The normalized temperature and the heat transfer coefficients are defined as:

$$(3.11)$$

Another approach is to use the local recovery temperature T_{rec} as the   characteristic fluid temperature which results in the following definitions.

$$(3.12)$$

The recovery temperature is defined as the steady state surface   temperature at adiabatic

conditions.

Goldstein and Behbahani (1982) recommended using the second approach, since the first approach results in the heat transfer coefficient being dependent on heat flux q. They showed the difference between the two approaches for the jet of uniform temperature identical to the temperature of the surrounding fluid. At a low Reynolds number (Re=35,200) when the total temperature in the jet was close to the recovery temperature, there was little difference between the two approaches. But the difference was significant near the stagnation region at high Reynolds number (Re=121,000).

Figure 3.16 shows the nozzle exit temperature distributions for the configuration described in figure 3.1. The temperature is normalized by the maximum jet temperature T_{jmax} and the initial wall temperature T_i. The results for three different Reynolds numbers fall onto a unique profile. The maximum temperature appears at the jet centerline. It was approximately 60, 55, and 50 ^{0}C for Re=30,000, 40,000 and 50,000, respectively, at 23 ^{0}C ambient temperature. It is quite obvious that the entrainment of the cold surrounding air to the heated jet tends to cool the jet as they move toward the impingement plate. The heating potential of the jet will be reduced and finally disappear far away from the stagnation region by the cooling effect of the entrained fluid. Thus the heating potential should be considered as the temperature difference $(T_{rec}-T_w)$ instead of $(T_{jmax}-T_w,)$ especially for the jet of the nonuniform temperature which is different from the surrounding fluid temperature.

The radial distributions of recovery temperature are measured for Re=30,000 in figure 3.17 for various H/D values. The steady state adiabatic condition was achieved after a two-hour continuous run. The recovery temperatures near the stagnation point are the same for both H/D=2 and 4, since the potential core like region extends to around five diameters downstream of the nozzle exit. They start to show a small decrease at H/D=6. The heating potential decreased a lot due to the entrainment of the cold surrounding air at H/D=6 and 8. At large distances from the stagnation point, the entrainment effect appears significant even for a very short nozzle-to-plate distance. The recovery temperatures of the wall layer region are relatively smaller than those of the stagnation point. Figures 3.18 and 3.19 show the Reynolds number effect on the recovery temperature distribution at H/D=4 and 6, respectively. The Reynolds number effect is shown to be negligible.

Figure 3.20 shows the results of temperature history measurement when the heated jet is suddenly allowed to impinge on the plate. Temperatures are measured through four thin foil K-type thermocouples at 4 separate radial locations from the stagnation points for Re=30,000 and H/D=4. Each temperature profile shows a nearly parabolic increase in time. Local heat flux histories are constructed from the temperature histories with the integral relation, equation (3.7). Then the heat transfer coefficients are obtained and non-dimensionalized by using equation (3.11). The Nusselt numbers shown in figure 3.21 decrease with time at each specific radial location. This tendency indicates that the heat transfer coefficient defined with the jet exit maximum temperature (h') is a function of the value of local heat flux. Nusselt numbers are also obtained through the error function relation, equation (3.8), and compared with the integral

relation results. Error function relation, which is used for the data reduction from liquid crystal images, is derived with the assumption of constant heat transfer coefficient. Figure 3.21 tells that the slight violation of the assumption does not have much effect on the heat transfer coefficient results. The heat transfer coefficients are also computed by using equation (3.12) and plotted in figure 3.22. Nusselt numbers are nearly constant in time during our transient experiment for each radial location. This fact leads us to the conclusion that the actual heating potential is the temperature difference between the local recovery temperature and the wall temperature. And, of course, the heat transfer coefficients defined with the recovery temperature are more universal than those with jet maximum temperature. Integral relation results and error function relation results also show an excellent agreement.

Convective heat transfer coefficients are obtained from time stamped color images, using the hue-capturing technique. Figure 3.23 shows the Nusselt number distribution obtained using 15 individual color images sampled at different times. The first image was captured at t=7.9 sec. from the beginning of the transient experiment and the last image was taken at t=88.1 sec. The multiple temperature points, corresponding to many of the colors which could be captured simultaneously with the present technique, improve the spatial resolution of the final heat transfer coefficient distribution greatly, compared to the previous techniques which provided only one single temperature point per video frame. The present method as shown in figure 3.23 provides more than 300 individual heat transfer coefficient measurements by using very accurately calibrated color information assigned to each pixel in the image. The initial wall temperature was uniformly distributed over the plate at an ambient level. The initial wall temperature uncertainty was approximately   0.1 ^{0} C. The elapsed time measurement was performed by using an electronic counter. The time measurement uncertainty including the very initial transient flow establishment time was $\pm$ 2 milliseconds.   This is extremely small compared to the typical time scale of the experiment which is in the order of seconds. The overall uncertainty of the Nusselt number was estimated to be $\pm$ 5.75 % using the standard uncertainty prediction method as described in appendix D. In this figure, the Nusselt number based on jet exit maximum temperature (Nu'), shows much smaller values than the Nusselt number defined by recovery temperature (Nu), especially at large radial distances from the stagnation point. The reason is that the heating potential is decreased much more in the outer region due to the entrainment.

Local Nusselt numbers measured using thermocouples and the new   liquid crystal technique are compared in figure 3.24. The hue-capturing technique results agree well for all the radial locations with the thermocouple results based on the integral relation which is known as a reliable method. Liquid crystal tests were performed twice for the same Reynolds number and the nozzle-to-plate distance. The liquid crystal results also show an excellent repeatability.

Local Nusselt number results of the current hue-capturing technique are also compared with the other studies investigated by conventional tools in figure 3.25. Considerable differences in Nusselt numbers exist among those results.   This discrepancy may be caused by the differences in the nozzle exit conditions, e.g., the mean velocity profile and the turbulence level.

Gardon and Cobonpue (1962) measured local heat transfer rate of an impinging jet discharged by a nozzle of well rounded inlet and short parallel throat with a steady state heat flux sensor. Obot et al. (1979) obtained heat transfer coefficients through thermocouple measurements of the wall temperature with known constant heat flux. They investigated the effect of the nozzle shape to the flow and heat transfer characteristics of impinging jets. Figure 3.25 includes the results of Obot et al. from three different nozzle geometries:

(1) *well contoured inlet, the nozzle length to diameter ratio, $l_n/D=1$;*
(2) *sharp edged inlet, $l_n/D =1$;*
(3) *sharp edged inlet, $l_n/D=10$.*

They concluded that the difference in nozzle geometry results in different free jet turbulence levels and mean velocity profiles, which in turn affects heat transfer coefficients. And the discrepancy may be attributed to the different temperature conditions. Both previous researches were performed with jets of ambient temperature and heated plate which cause negligible entrainment effect, while our results were obtained with nonuniform heated jet and the plate of ambient initial temperature. However, all the results show a similar trend with the second maximum around two nozzle diameters away from the stagnation point.

Figure 3.26 shows the effect of the nozzle-to-plate distance on the heat transfer coefficients for Re=30,000. The overall magnitude of Nusselt numbers show only a slight variation to the distance change due to the non-dimensionalization effect of the recovery temperature. Nusselt numbers decrease monotonically along the radial direction with the maximum at stagnation point for long nozzle-to-plate distance, H/D=6 and 8. For H/D=4, the second maximum in Nusselt number appears around two diameters away from the stagnation point. Amano (1983) attributed the second peak to high near wall turbulent kinetic energy around r/D=2. The high near wall turbulent intensity at r/D=2, is also shown in figure 3.15. While Sparrow et al. (1975) attributed this to transition from laminar to turbulent flow, the mechanisms causing this feature are still not clear. This dispute could be solved through a more detailed investigation of turbulent and heat transport mechanism in the near wall region. Reynolds number effects on heat transfer characteristics are investigated in figure 3.27 and 3.28 for H/D=4 and 6, respectively. Both results show significant increase in Nusselt numbers with Reynolds number.

III . 4   Conclusions

A liquid crystal based temperature and heat transfer measurement approach using a transient method is described. A round impinging jet on a flat surface is used as a test case to

evaluate the overall procedure. Although the current study describes the development of a transient temperature and heat transfer measurement approach, it is comprehensively supported by fluid mechanics observations both in the free jet region and in the near wall region of the impingement plate.

The local Nusselt number histories were obtained from the temperature history measurements with fast response surface mounted thermocouples for the validation of the results from the color recognition based approach used in the present study.

The Nusselt numbers based on the jet exit maximum temperature decreased with time at each specific radial location; while the Nusselt numbers based on the recovery temperature were nearly constant in time. It was concluded that the actual heating potential was the temperature difference between the local recovery temperature and the wall temperature. The heat transfer coefficients defined with the recovery temperature were found to be independent of the thermal boundary conditions of the forced convection problem.

When constructing wall heat flux from the surface temperature time history, the error function relation results agreed well with the convolution integral relation results. The convolution integral relation proved that the heat transfer coefficient was constant in time when the heating potential was defined with the recovery temperature. This feature allowed the use of a single time point solution represented by an error function, for liquid crystal data reduction.

The heat transfer coefficients on the impingement plate were obtained both from the liquid crystal thermography and surface mounted discrete thermocouples. Local Nusselt number results from the color recognition (hue capturing) approach compared very well with the thermocouple based measurements at discrete points. The liquid crystal based results showed excellent repeatability.

Local Nusselt number results from the liquid crystal thermography were also compared to other impinging jet heat transfer studies using conventional techniques. In general, the results from the color recognition based (hue capturing) method agreed well with the results available from the literature.

As a result of a set of experiments, it has been shown that the new hue capturing method implemented in a transient heat transfer model is an accurate and powerful tool in mapping surface heat transfer coefficients with high resolution. The method is non-intrusive and the overall uncertainty on convective heat transfer coefficient from the specific technique is estimated to be 5.7 %.

References

Baughn, J. W., Ireland, P. T., Jones, T. V. and Saniei, N., "A Comparison of the Transient and

Heated-Coating Methods for the Measurement of Local Heat Transfer Coefficients on a Pin Fin," ASME Paper 88-GT-180, 1988.

Camci, C., Kim, K. and Hippensteele, S. A., "A New Hue Capturing Technique for the Quantitative Interpretation of Liquid Crystal Images Used in Convective Heat Transfer Studies," ASME Paper 91-GT-277, 1991, to be published in Trans. of the ASME, J. of Turbomachinery.

Gardon, R. and Akfirat J. C., "The Role of Turbulence in Determining the Heat-transfer Characteristics of Impinging Jets," *Int. J. of Heat and Mass Transfer*, Vol. 8, pp. 1261-1272, 1965.

Gardon, R. and Cobonpue, J., "Heat Transfer between a Flat Plate and Jets of Air Impinging on It," International Developments in Heat Transfer, pp. 454-460, ASME, New York, 1962.

Goldstein, R. J. and Behbahani, A. I., " Impingement of a Circular Jet with and without Cross Flow," *Int. J. of Heat and Mass Transfer*, Vol. 25, pp. 1377-1382, 1982.

Goldstein, R. J., Behbahani, A. I. and Heppelmann, K. K., " Streamwise Distribution of the Recovery Factor and the Local Heat Transfer Coefficient to an Impinging Circular Air Jet," *Int. J. of Heat and Mass Transfer,* Vol. 29, pp. 1227-1235, 1986.

Goldstein, R. J., Sobolik, K. A. and Seol, W. S., "Effect of Entrainment on the Heat Transfer to a Heated Circular Air Jet Impinging on a Flat Surface," *Trans. of the ASME, J. of Heat Transfer*, Vol. 112, pp. 608-611, 1990.

Jones, J. J., Shock Tube Heat Transfer Measurements on inner Surface of a Cylinder (Simulating a Flat Plate) for Stagnation Temperature Range 4100 to 8300 ^{0}C," NASA TN-D-54, 1959.

Kline, S. J. and McClintock, F. A., "Describing Uncertainties in Single Sample Experiments," *Mechanical Engineering,* Vol. 75, pp. 3-8, 1953.

Obot, N. T., Majumdar, A. S. and Douglas, W. J. M., " The Effect of Nozzle Geometry on Impingement Heat Transfer under a Round Turbulent Jet," ASME Paper 79 WA/HT-53, 1979.

Saabas, H. J., Arora, S. C. and Abdel Messeh, W., " Application of the Transient Test Technique to Measure Local Heat Transfer Coefficients Associated with Augmented Airfoil Cooling Passages," ASME Paper 87-GT-212, 1987.

Schultz, D. L. and Jones, T. V., "Heat Transfer Measurements in Short Duration Hypersonic Facilities," AGARD-AG-165, 1973.

Sparrow, E. M., Goldstein, R. J. and Rouf, M. A., "Effect of Nozzle-surface Separation Distance on Impingement Heat Transfer for a Jet in a Crossflow," *Trans. of the ASME, J. of Heat Transfer*,
Vol. 97, pp. 528-533, 1975.

Striegl, S. A. and Diller, T. E., "An Analysis of the Effect of Entrainment Temperature on Jet Impingement Heat Transfer," *Trans. of the ASME, J. of Heat Transfer,* Vol. 106, pp. 804-810, 1984a.

Striegl, S. A. and Diller, T. E., "The Effect of Entrainment Temperature on Jet Impingement Heat Transfer," *Trans. of the ASME, J. of Heat Transfer,* Vol. 106, pp. 27-33, 1984b.

Treaster, A. L. and Yocum, A. M., The Calibration and Application of Five-hole Probes," *ISA Transactions*, Vol. 18, No. 3, pp. 23-34, 1979.
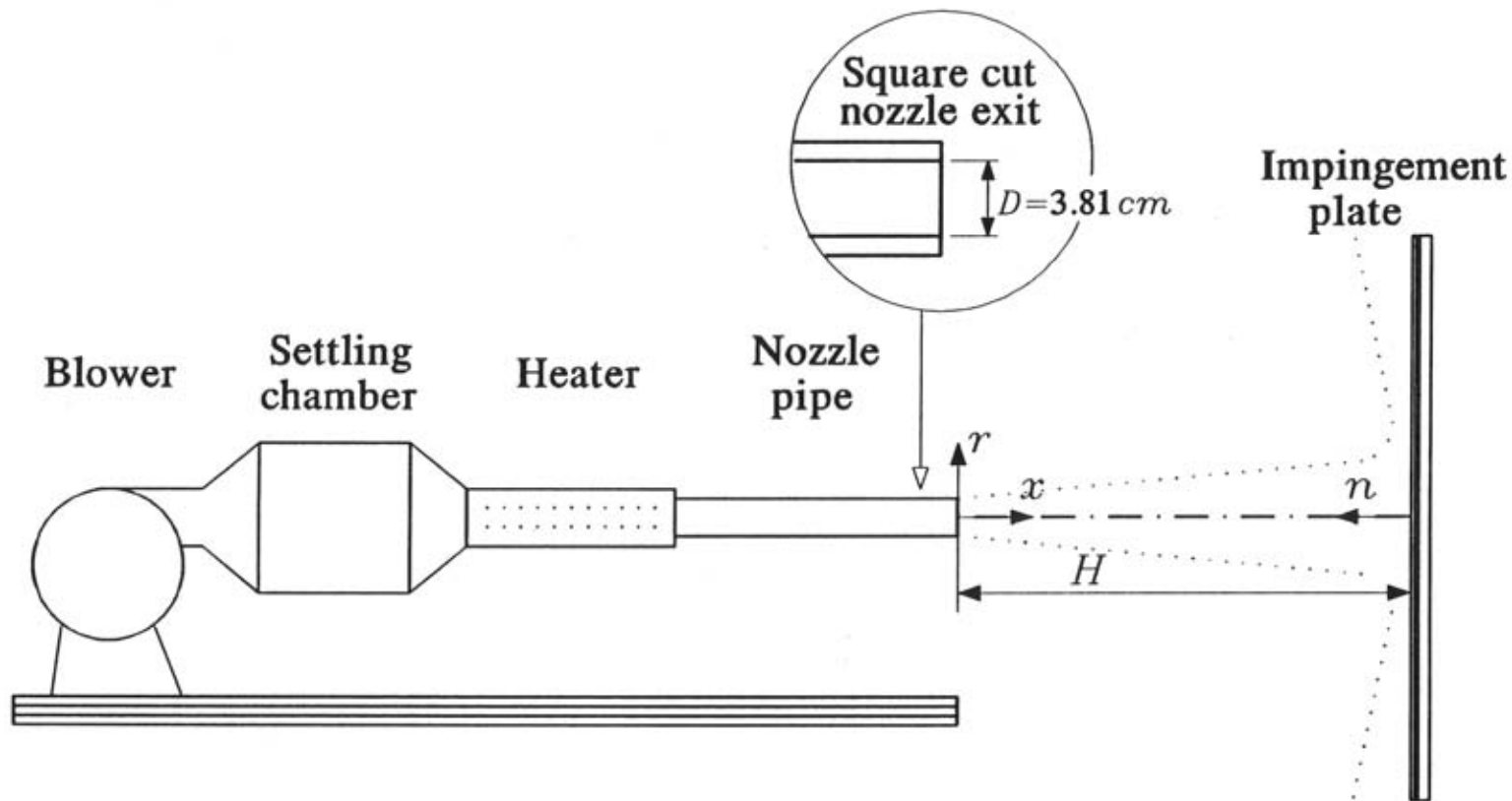
Figure 3.1 Schematic of the flow system.
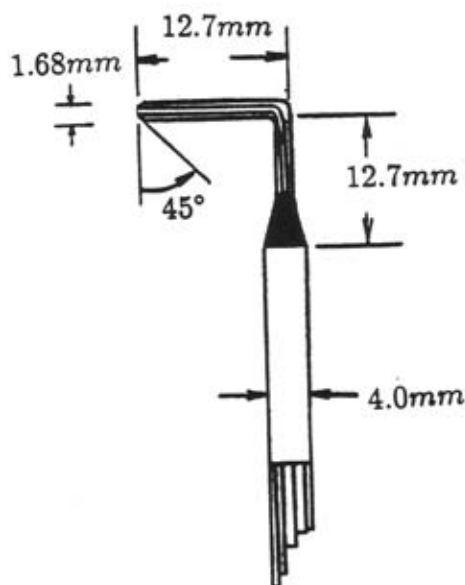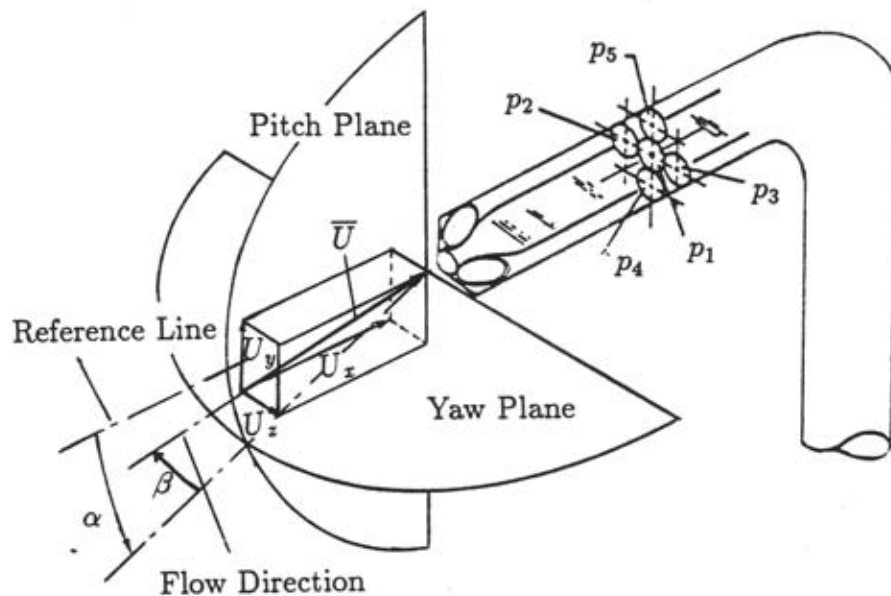
Velocity Vector Resolution

$$U_x = \overline{U} \cos \alpha \cos \beta$$

$$U_y = \overline{U} \sin \alpha \cos \beta$$

$$U_z = \overline{U} \sin \beta$$

Definitions of Calibration Coefficients

$$Cp_{yaw} = (p_2 - p_3)/(p_1 - \overline{p})$$

$$Cp_{pitch} = (p_4 - p_5)/(p_1 - \overline{p})$$

$$Cp_{total} = (p_1 - p_{total})/(p_1 - \overline{p})$$

$$Cp_{static} = (\overline{p} - p_{static})/(p_1 - \overline{p})$$

$$\overline{p} = (p_2 + p_3 + p_4 + p_5)/4$$

Figure 3.2 Geometric details of the five-hole probe and definitions of calibration coefficients.

(b)
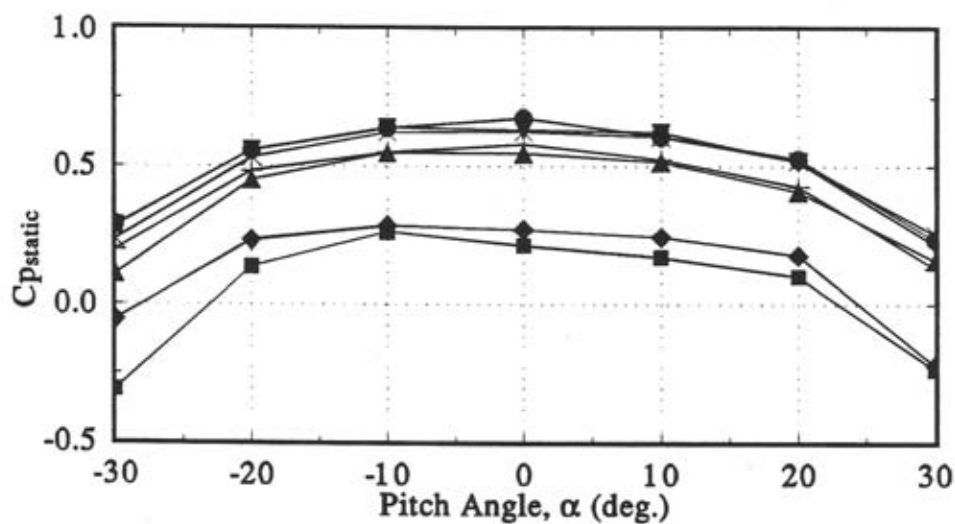
(c)
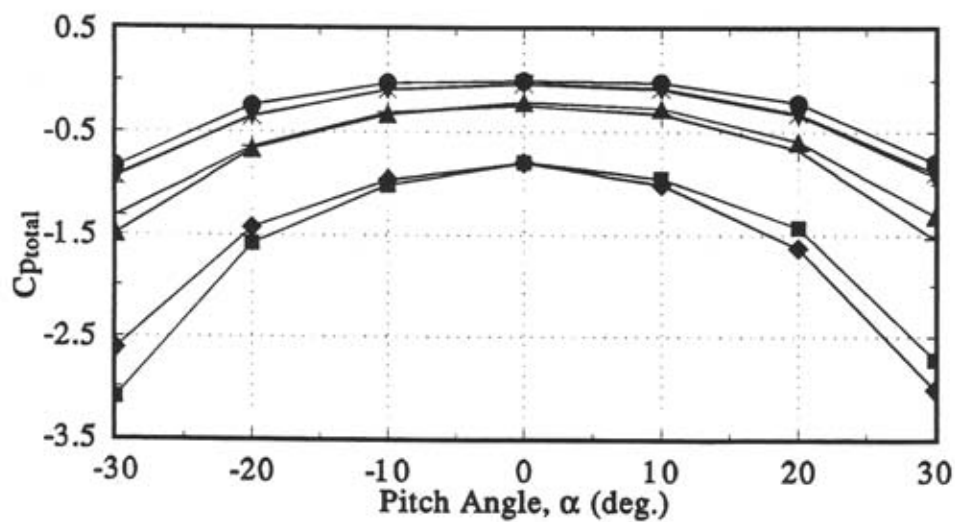
Figure 3.3 (continued).
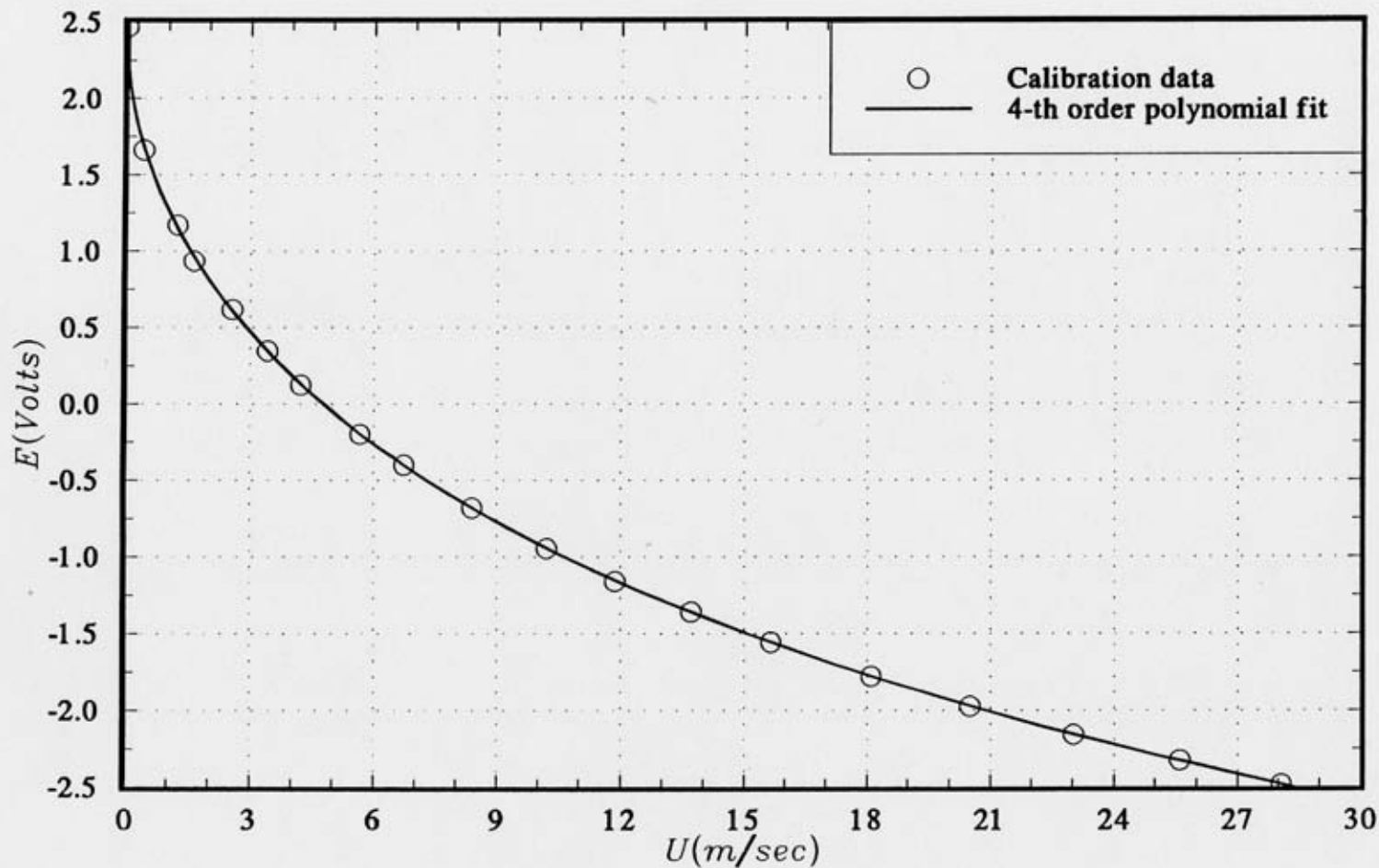
Figure 3.4 A typical calibration results of the hot-wire.

jet centerline velocity at the nozzle exit $= 16.8 m/sec$
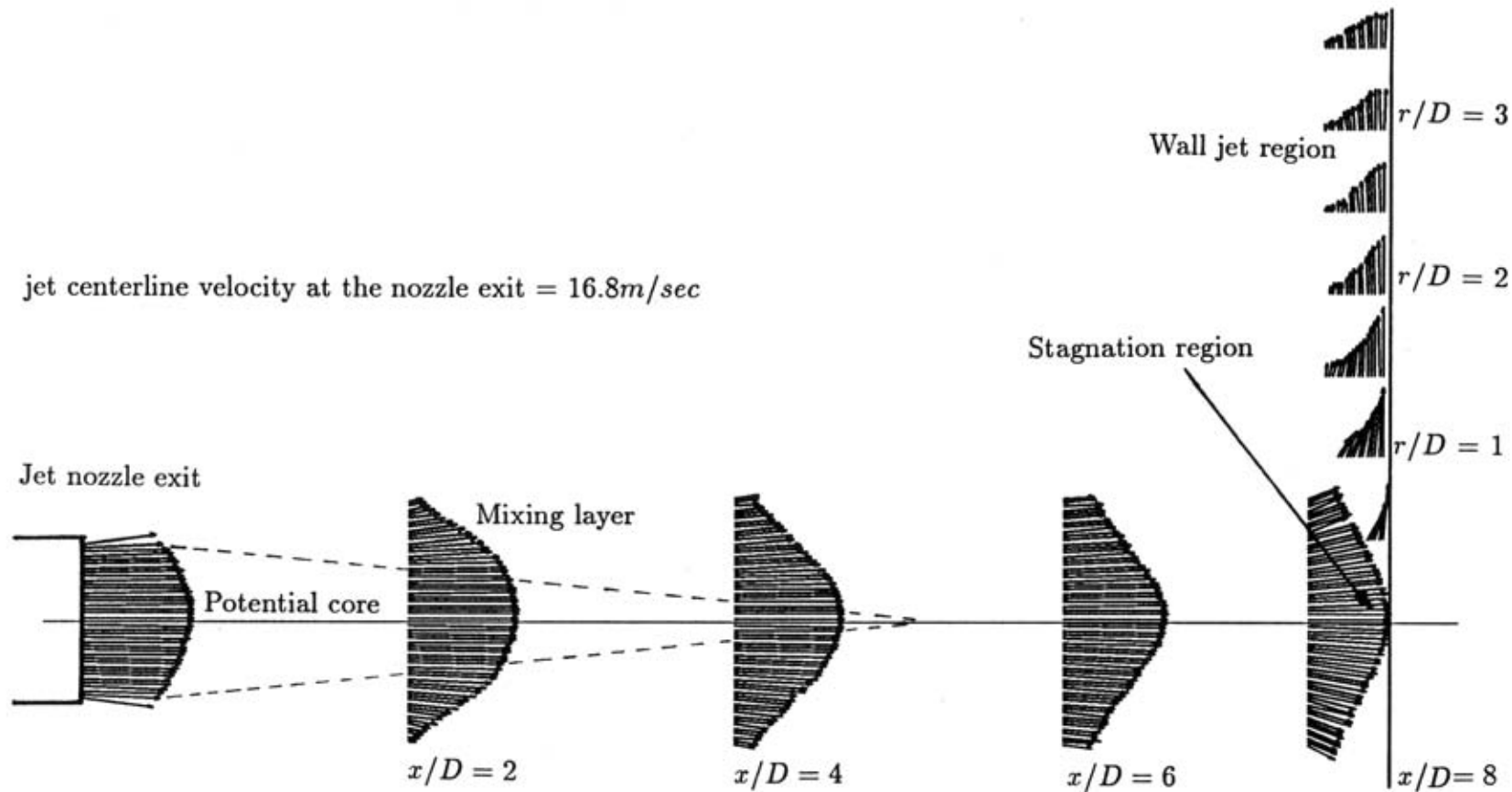
Figure 3.5 Velocity vector distributions measured through the five-hole probe, $Re = 30,000$, $H/D = 8$.

jet centerline velocity at the nozzle exit = 16.8 m/sec

$r/D = 3$

$r/D = 2$

$r/D = 1$

$x/D = 2$

$x/D = 4$
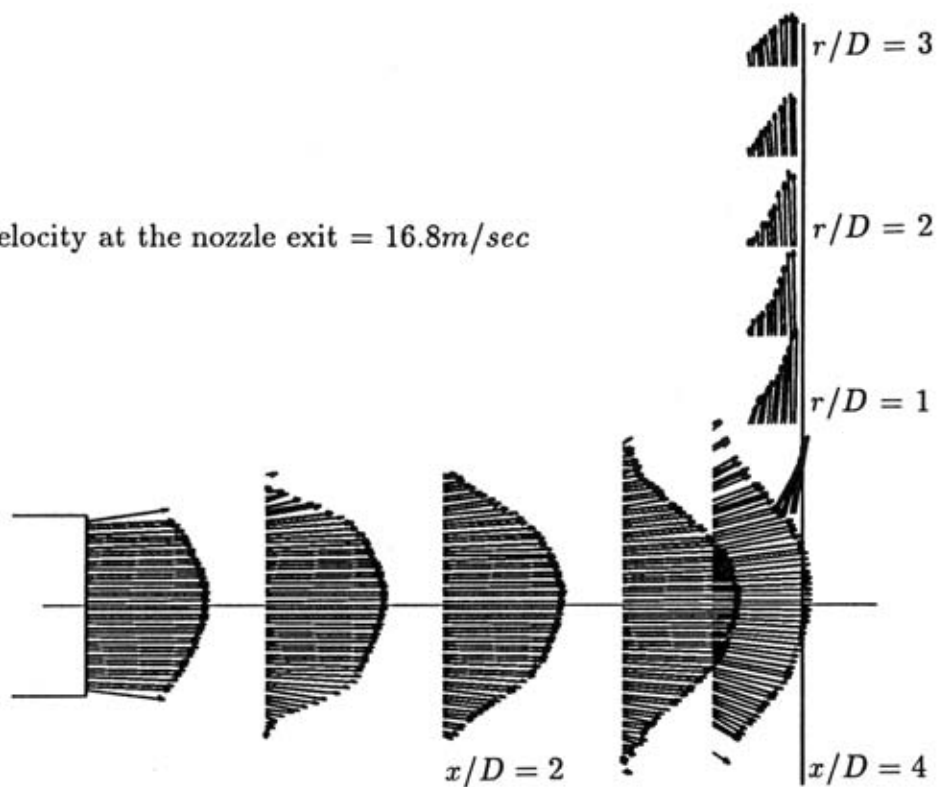
Figure 3.6 Velocity vector distributions measured through the five-hole probe, $Re = 30,000$, $H/D = 4$.

jet centerline velocity at the nozzle exit $= 22.4m/sec$

$r/D = 3$

$r/D = 2$

$r/D = 1$

$x/D = 2$

$x/D = 4$
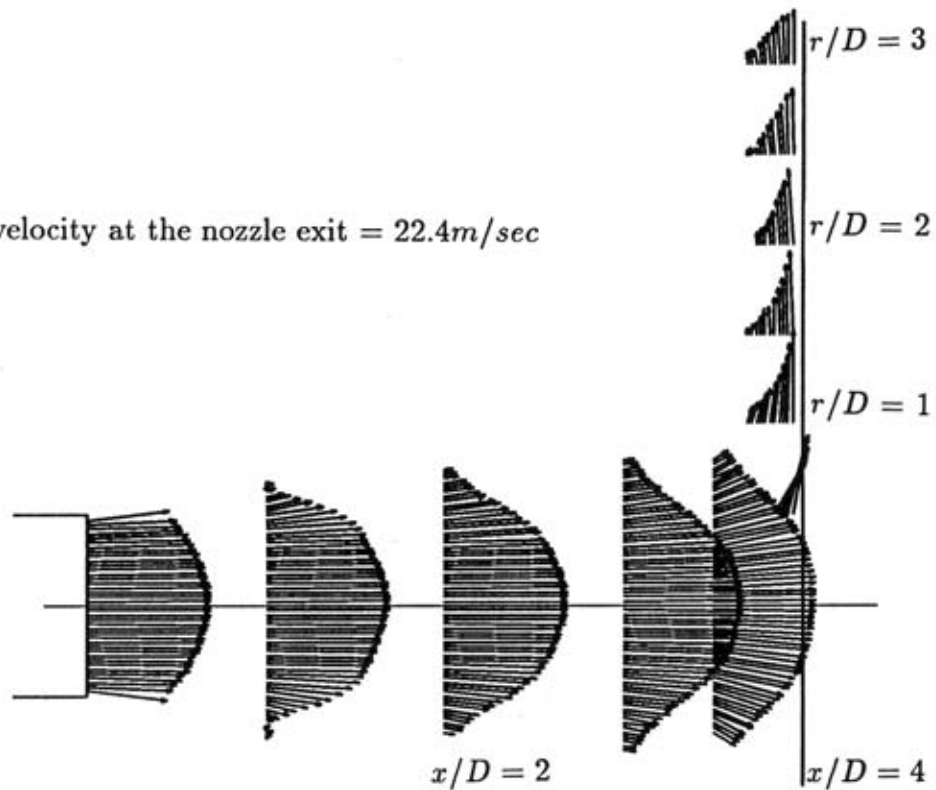
Figure 3.7 Velocity vector distributions measured through the five-hole probe, $Re = 40,000$, $H/D = 4$.
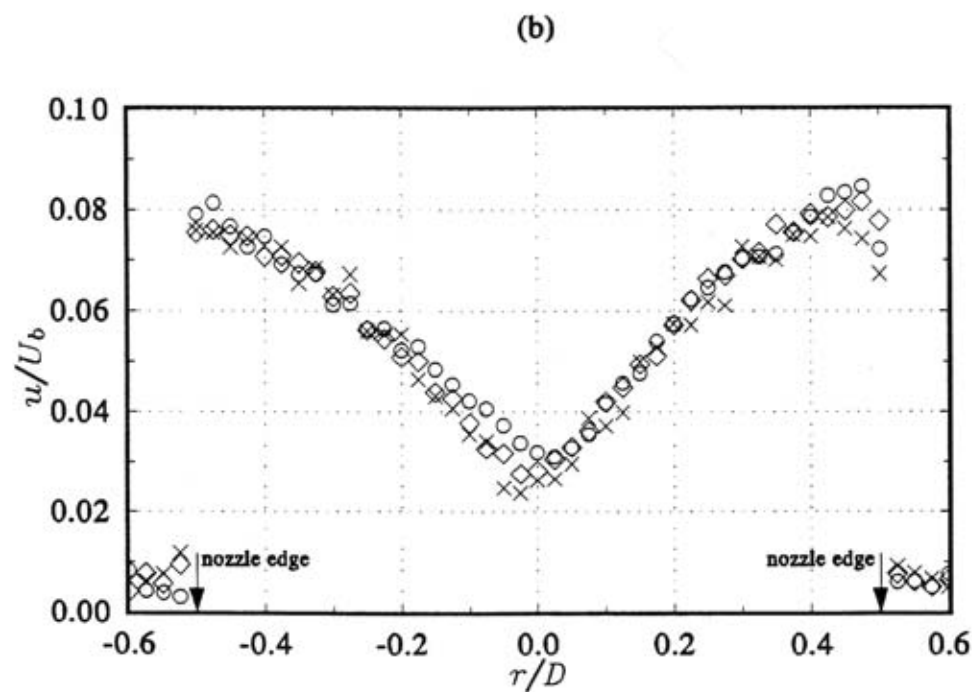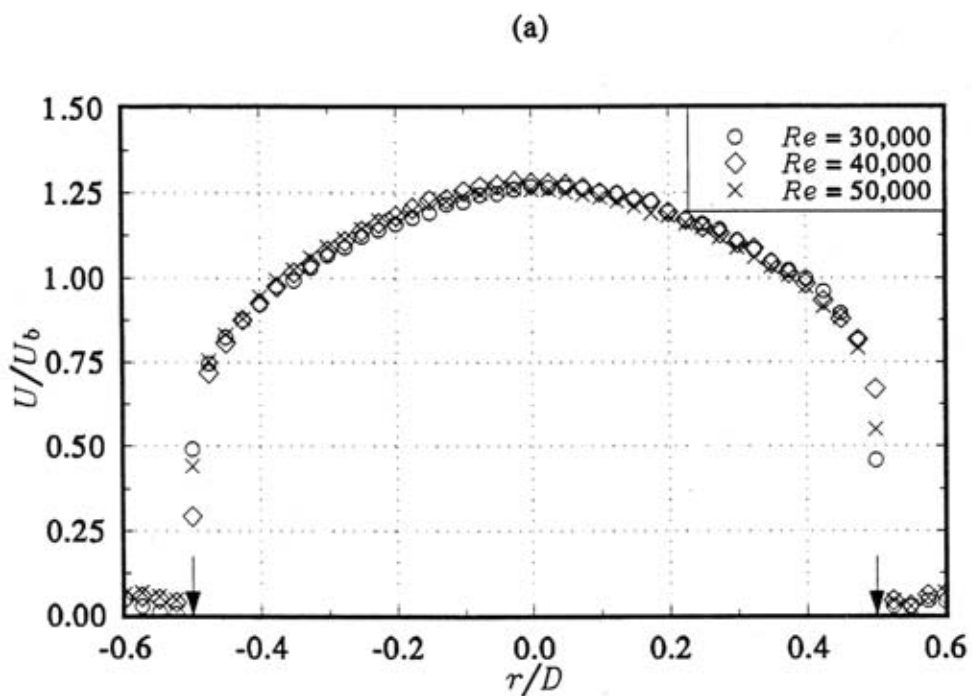
Figure 3.8 Hot-wire flow results measured at the nozzle exit, $H/D = 4$, (a) mean velocity, (b) turbulent intensity.

(a)

(b)
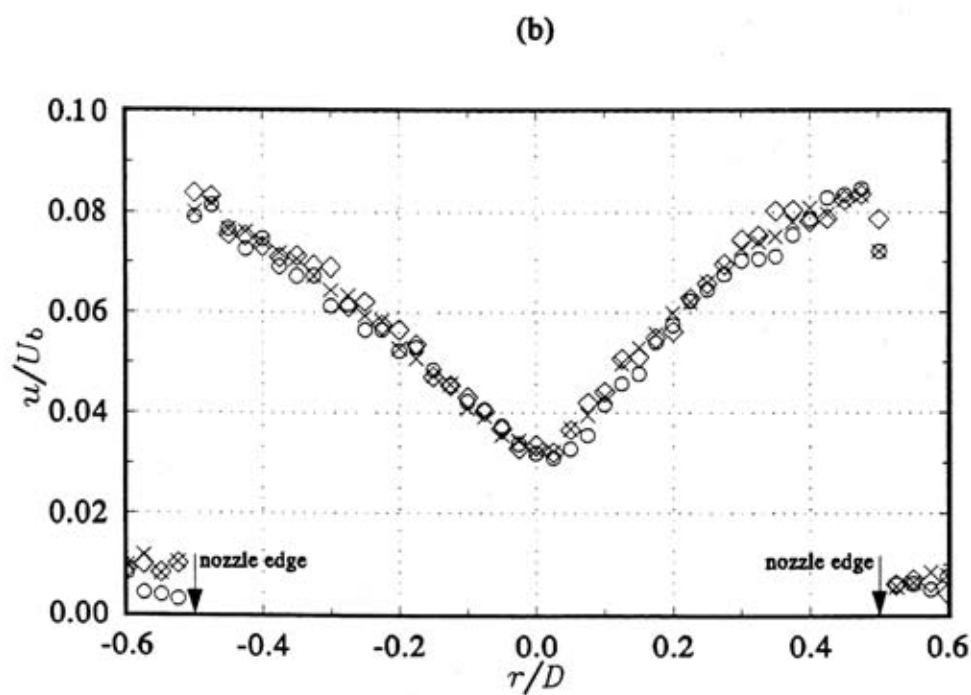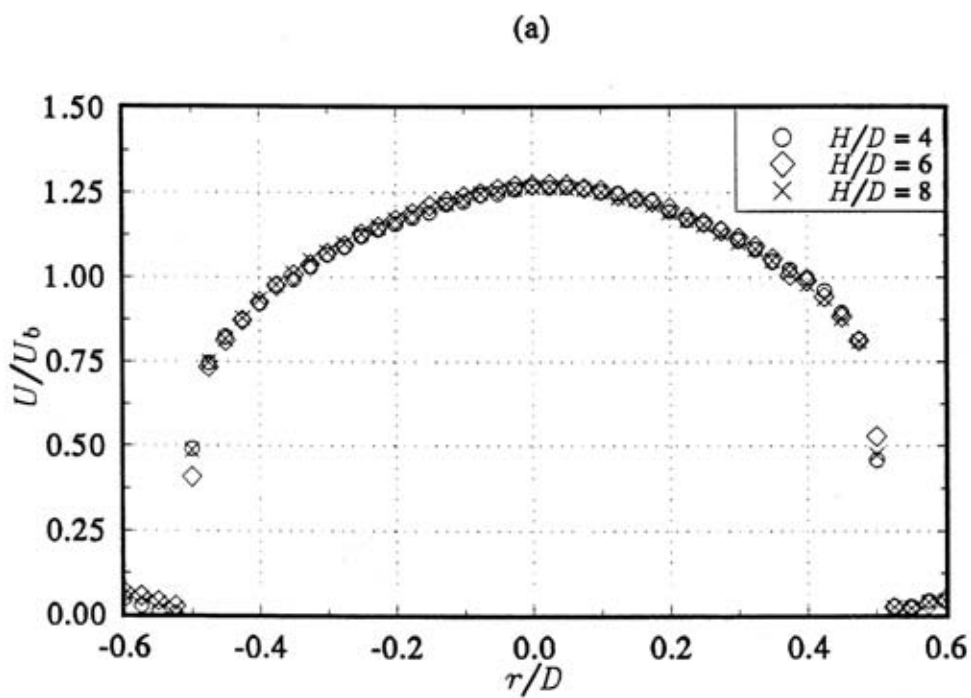
Figure 3.9 Hot-wire flow results measured at the nozzle exit, $Re = 30,000$,
(a) mean velocity, (b) turbulent intensity.

25

(a)
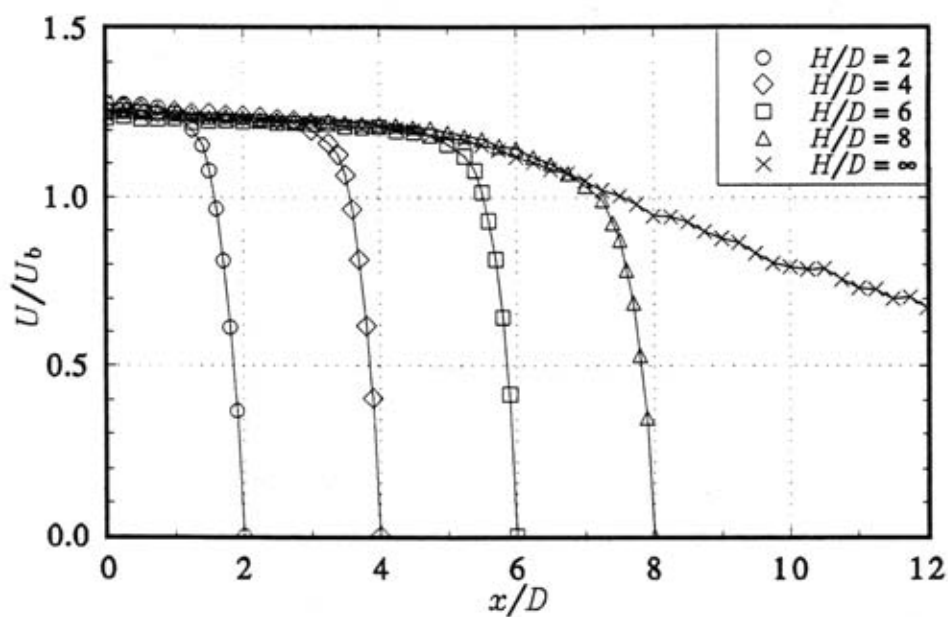
(b)
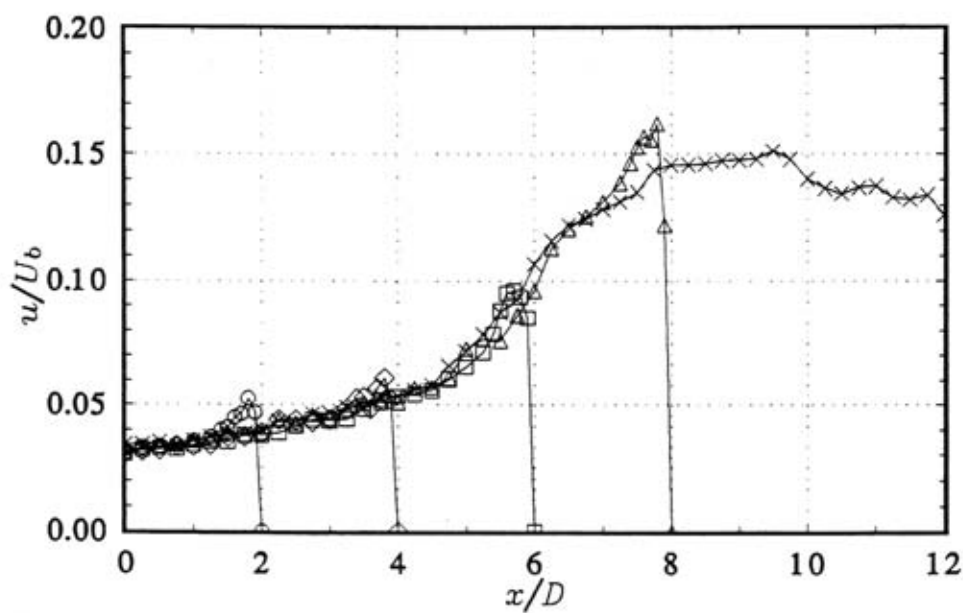
Figure 3.10 Hot-wire flow results measured along the jet centerline, $Re = 30,000$, (a) mean velocity, (b) turbulent intensity.

(a)
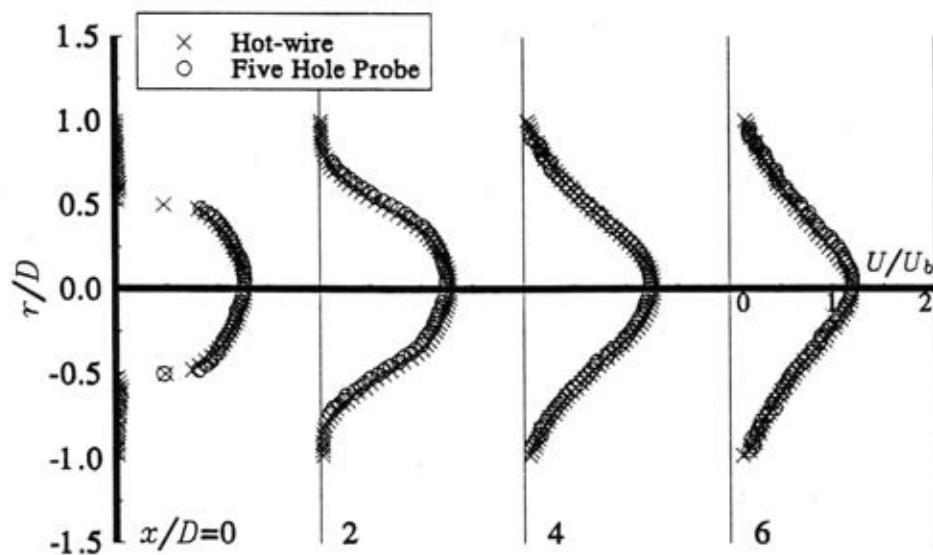
(b)
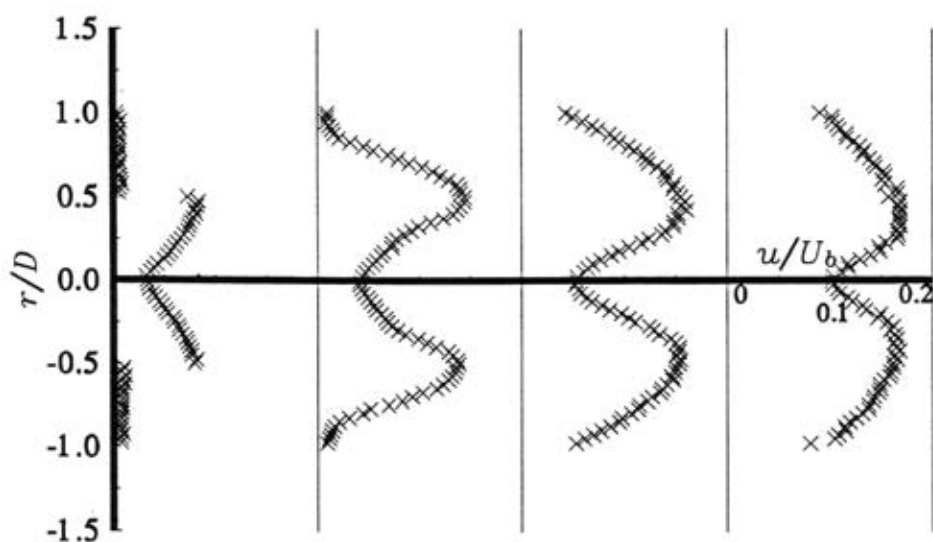
Figure 3.11 Radial distributions of (a) mean velocity and (b) turbulent intensity in the free jet region, $Re = 30,000$, $H/D = 8$.

(a)

x/D=0   1   2   3
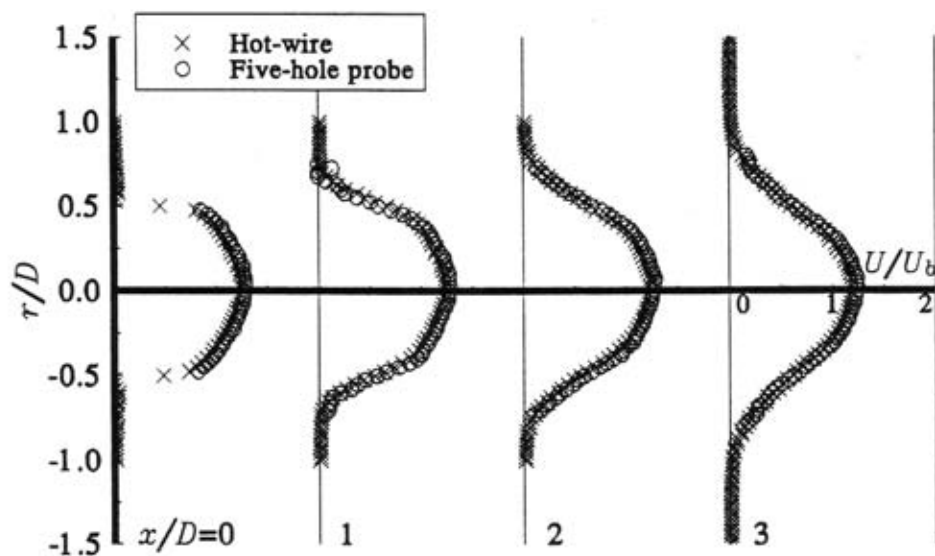
(b)
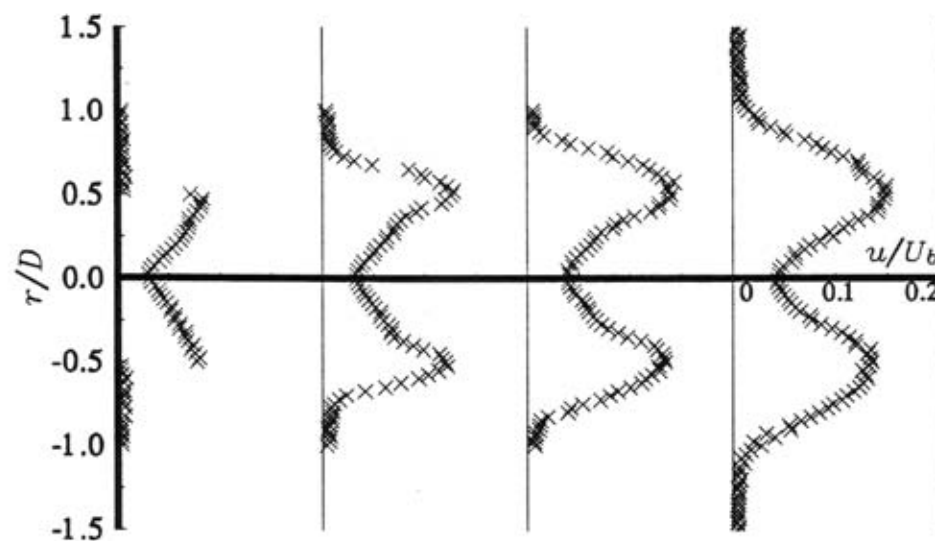
Figure 3.12 Radial distributions of (a) mean velocity and (b) turbulent intensity in the free jet region, $Re = 30,000$, $H/D = 4$.

28

(a)
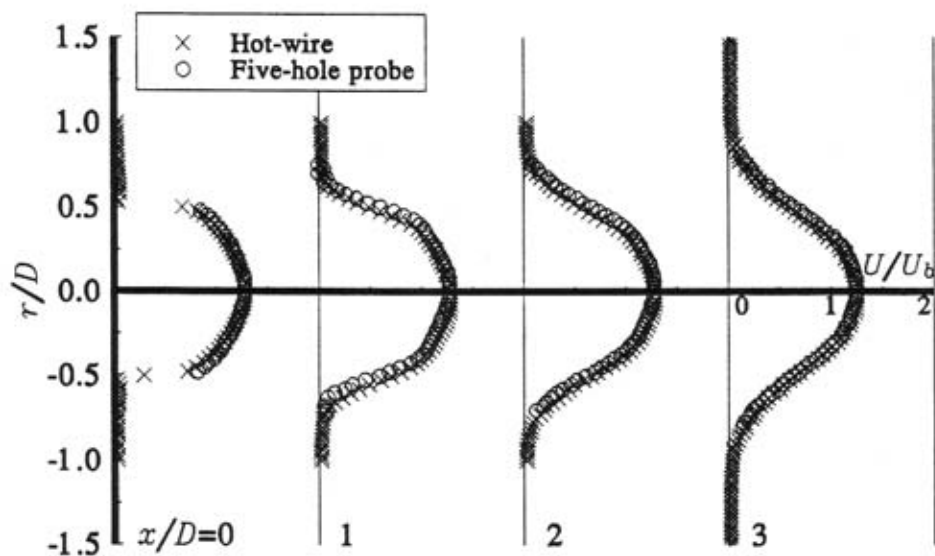
(b)
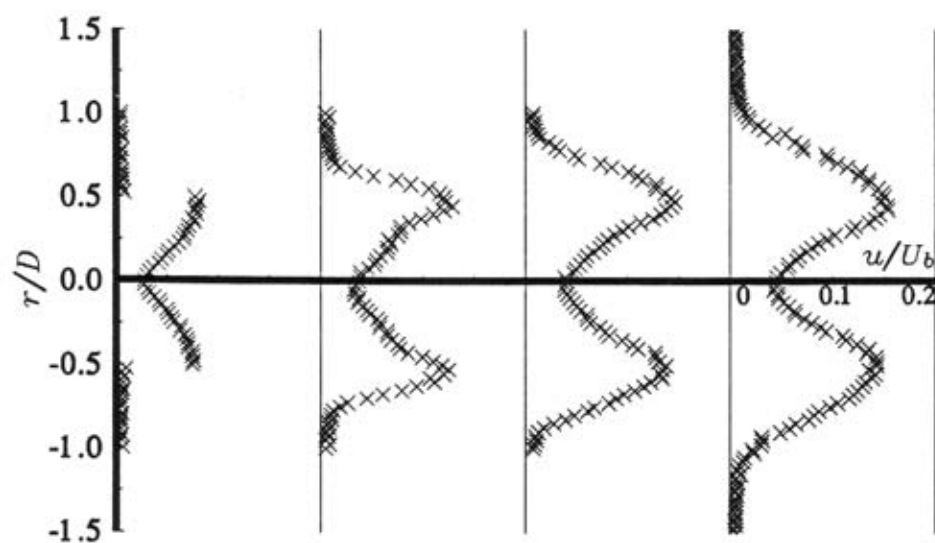
Figure 3.13 Radial distributions of (a) mean velocity and (b) turbulent intensity in the free jet region, $Re = 40,000$, $H/D = 4$.

29
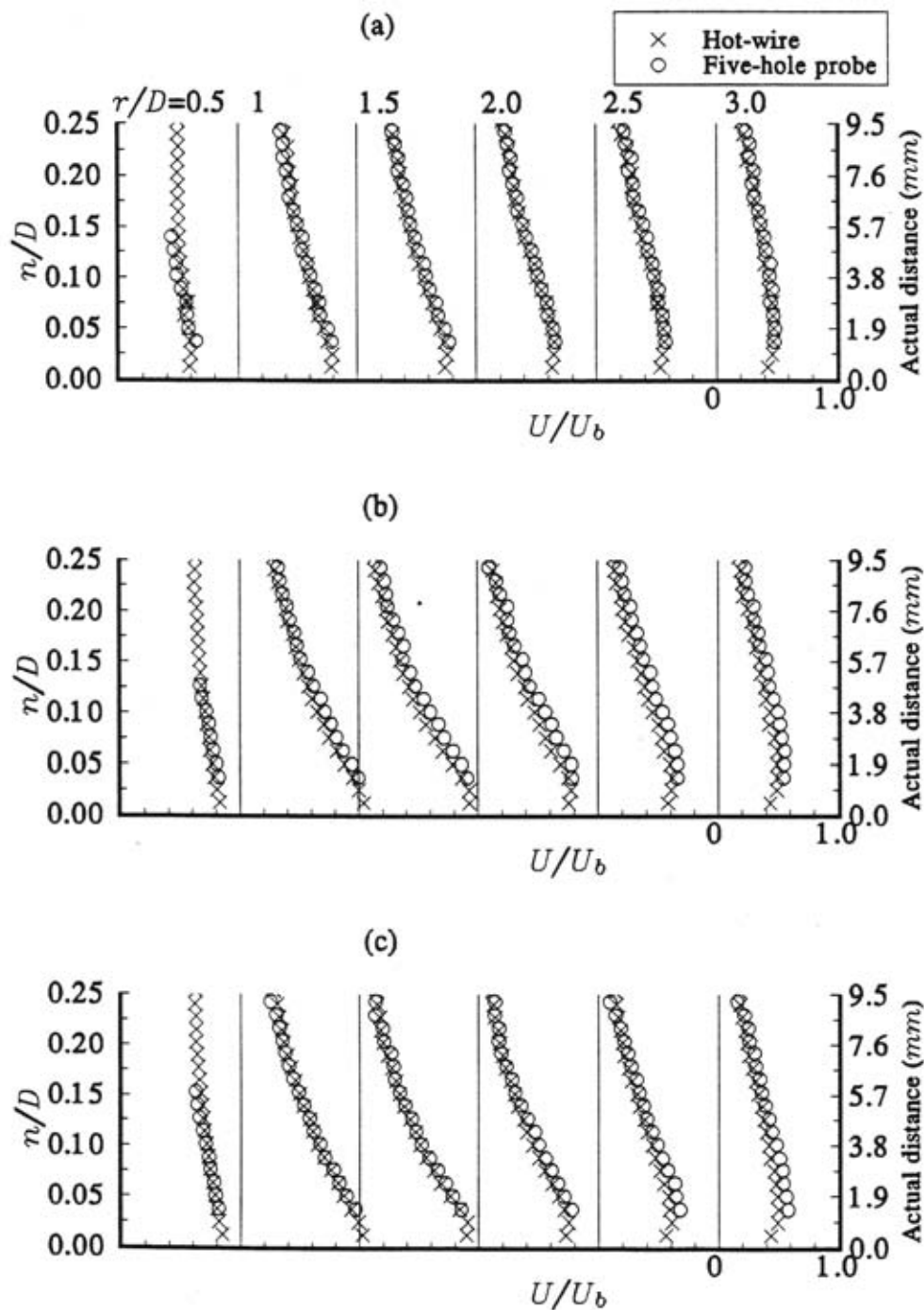
Figure 3.14 Mean velocity distributions in the wall jet region, (a) $Re = 30,000$, $H/D = 8$, (b) $Re = 30,000$, $H/D = 4$, (c) $Re = 40,000$, $H/D = 4$.

30
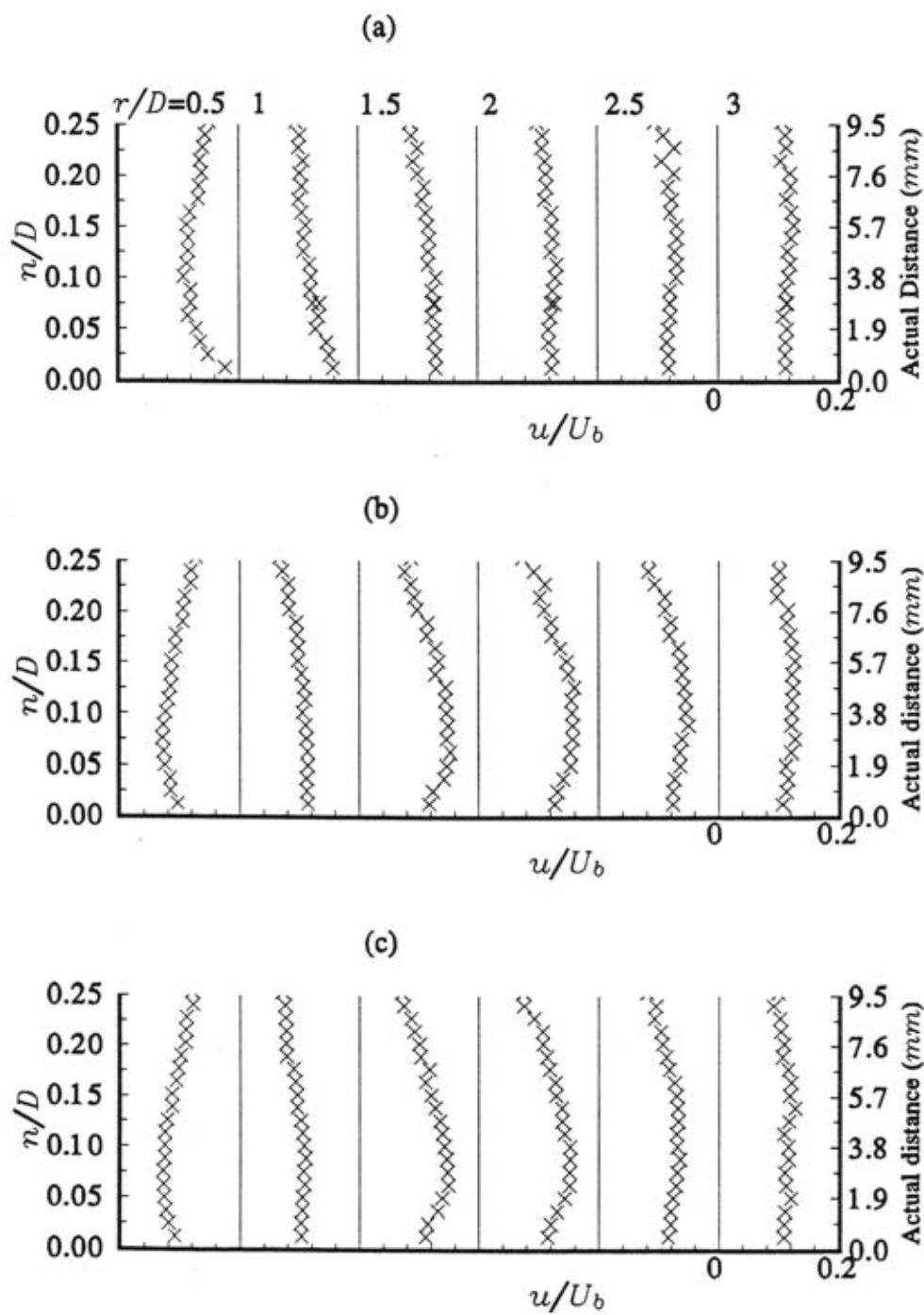
Figure 3.15 Turbulent intensity distributions in the wall jet region, (a) $Re = 30,000$, $H/D = 8$, (b) $Re = 30,000$, $H/D = 4$, (c) $Re = 40,000$, $H/D = 4$.
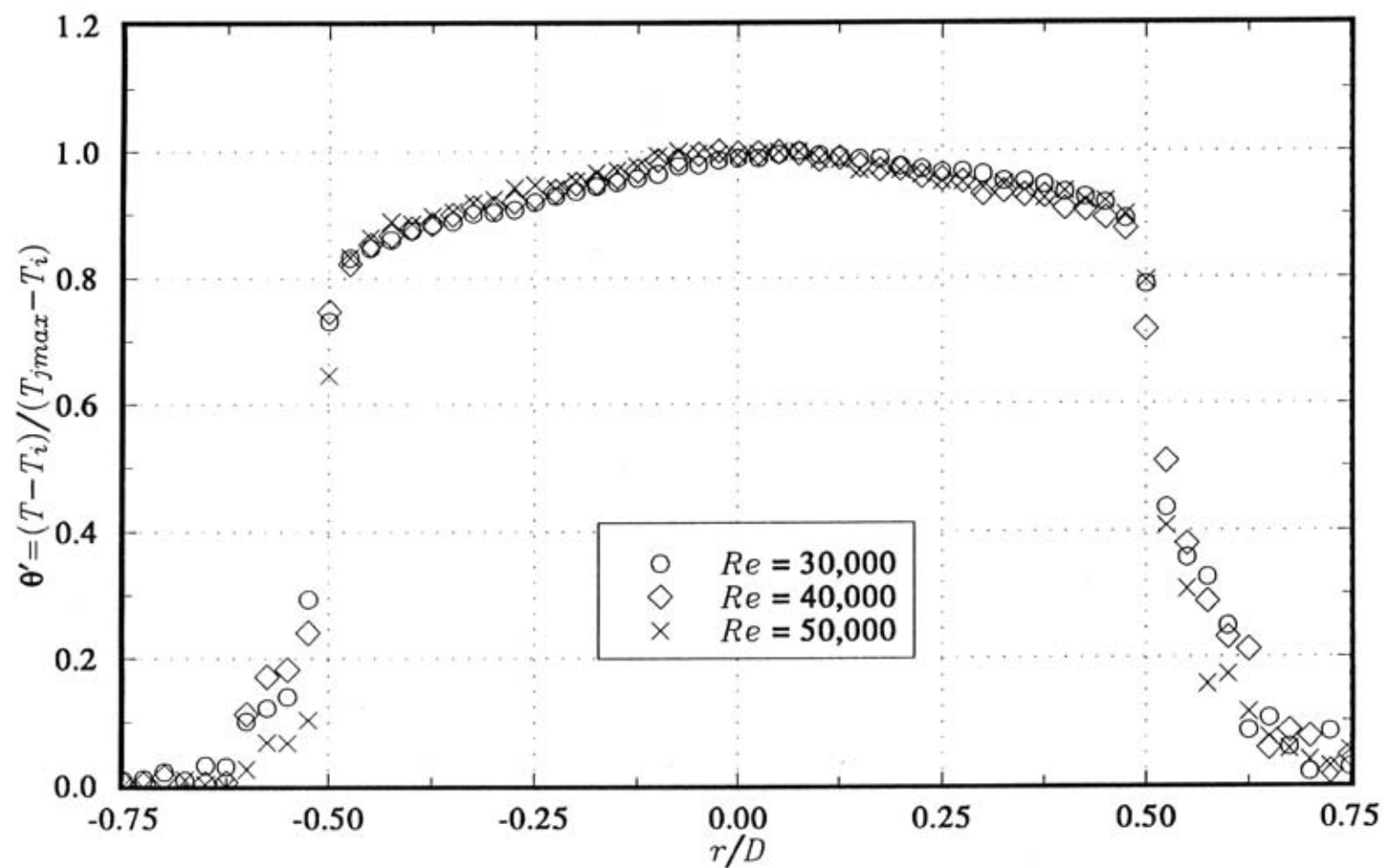
Figure 3.16 Temperature distributions measured at the nozzle exit.
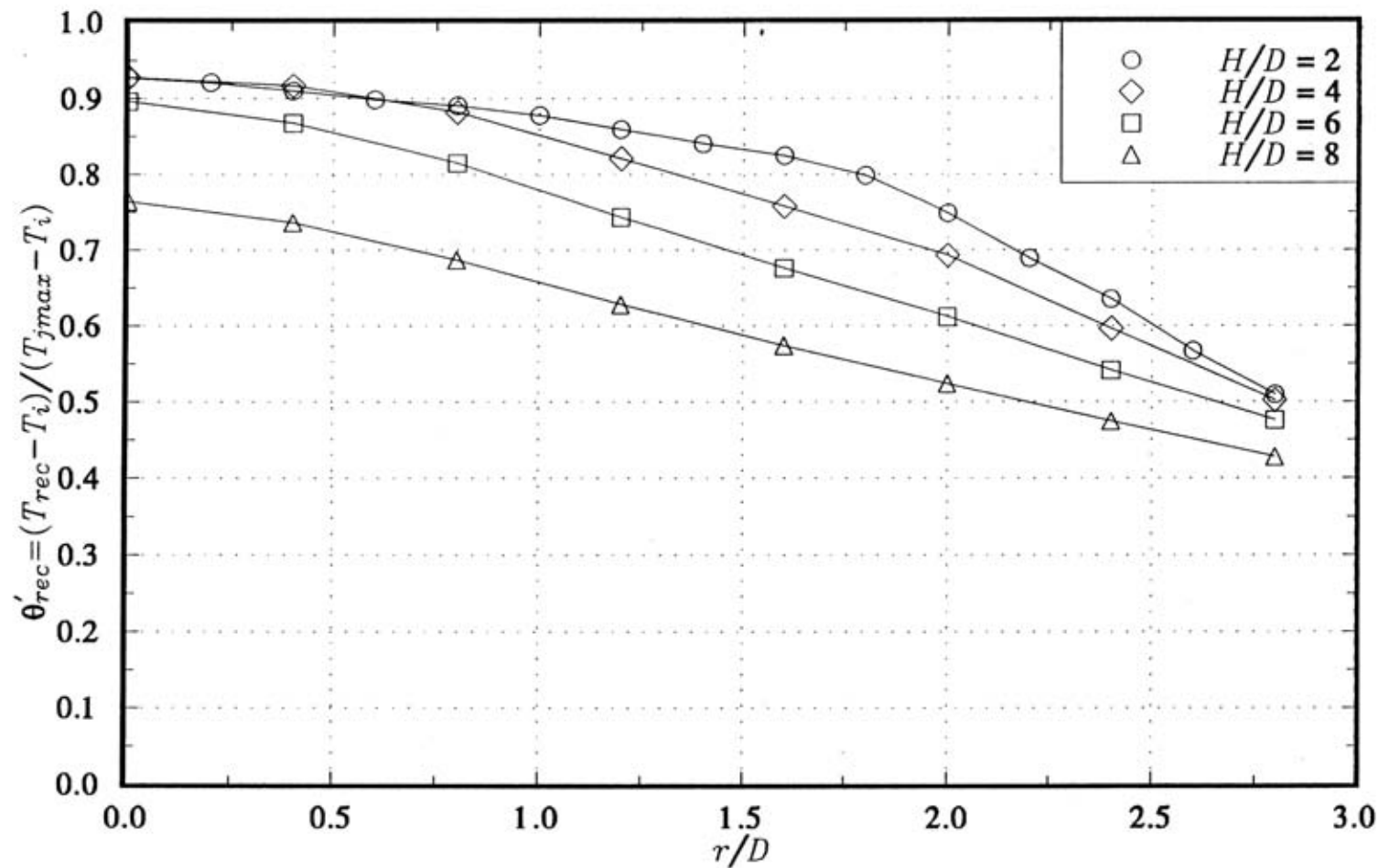
Figure 3.17 Radial distributions of recovery temperature, $Re = 30,000$.
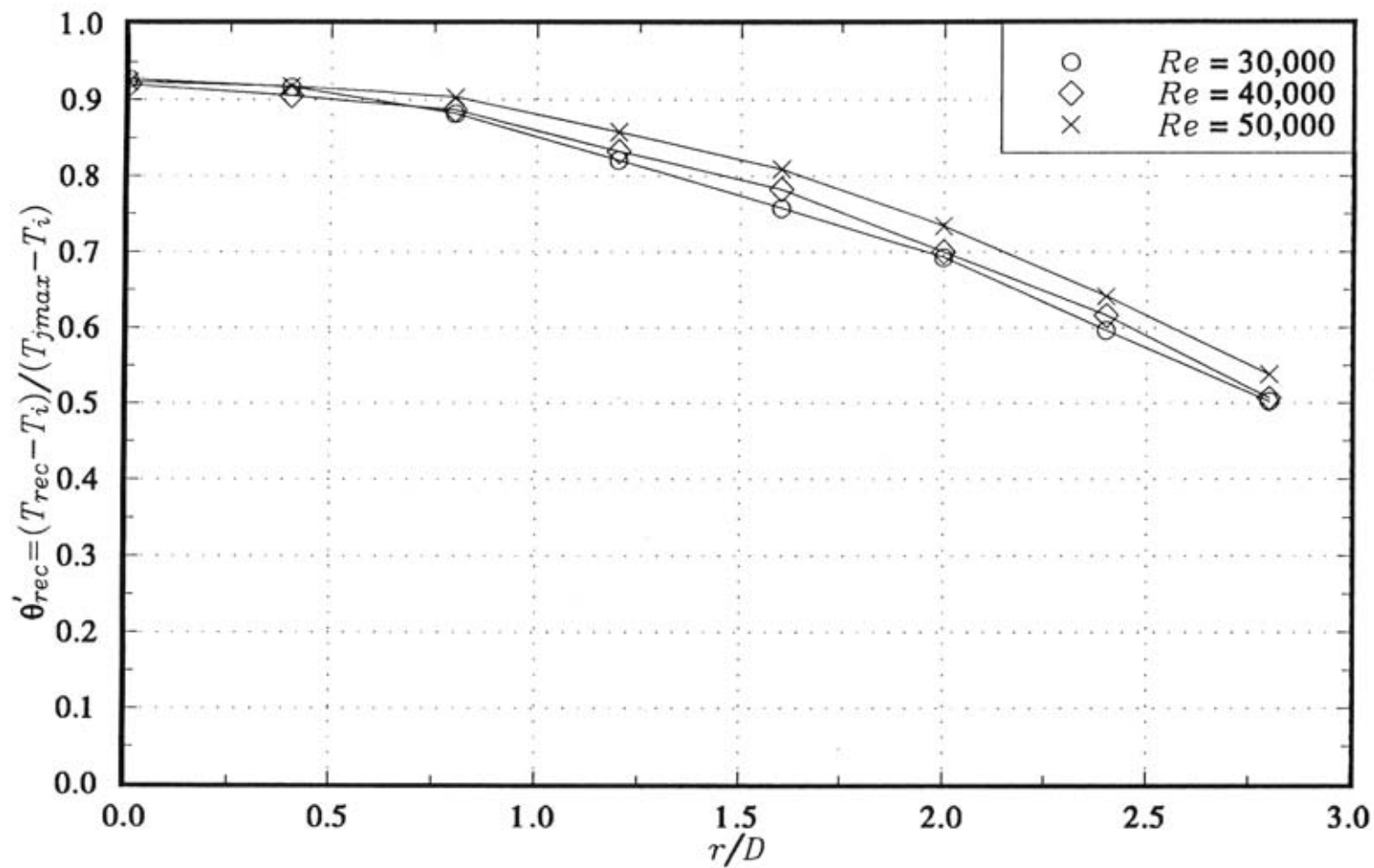
Figure 3.18 Radial distributions of recovery temperature, $H/D = 4$.
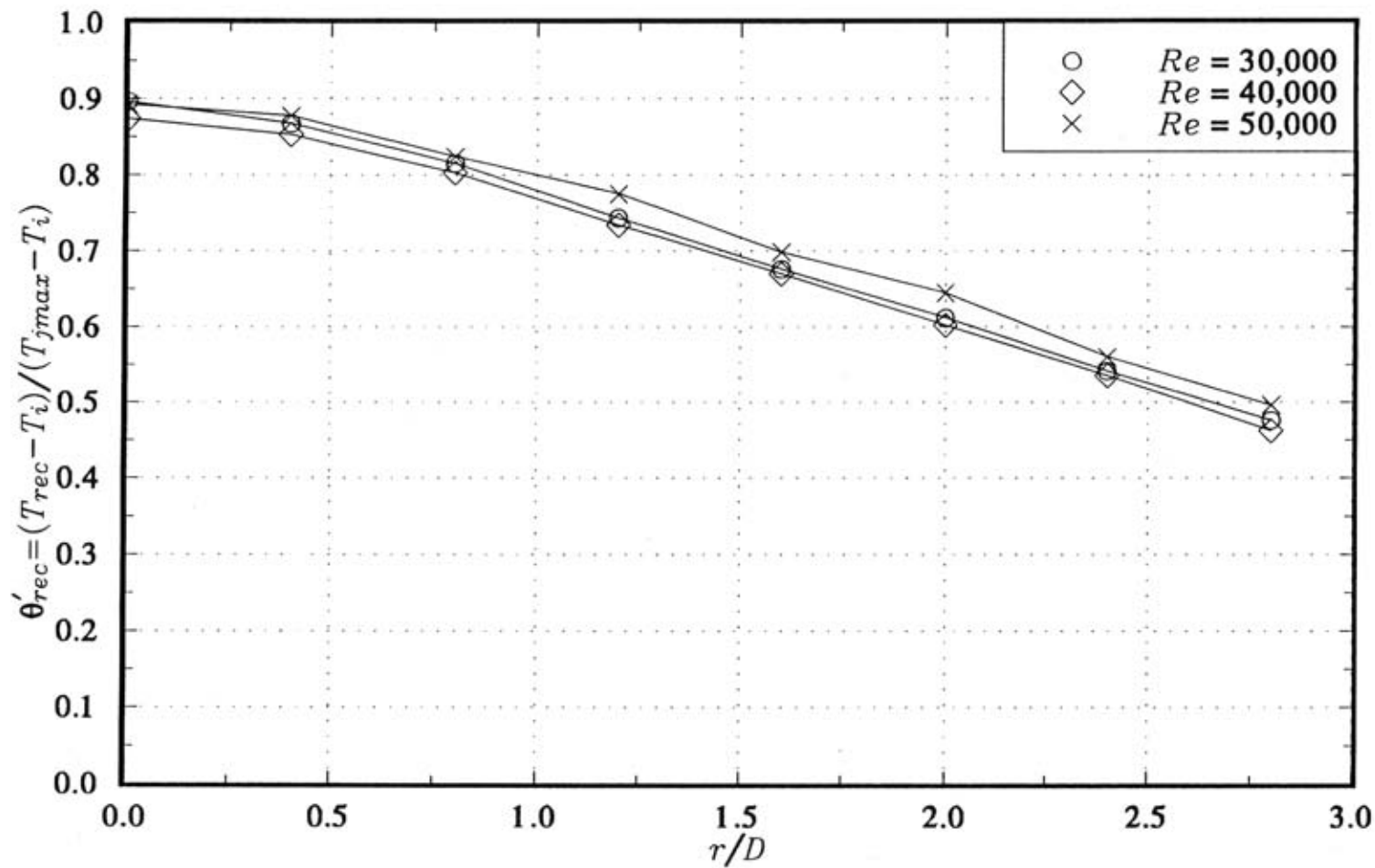
Figure 3.19 Radial distributions of recovery temperature, $H/D = 6$.
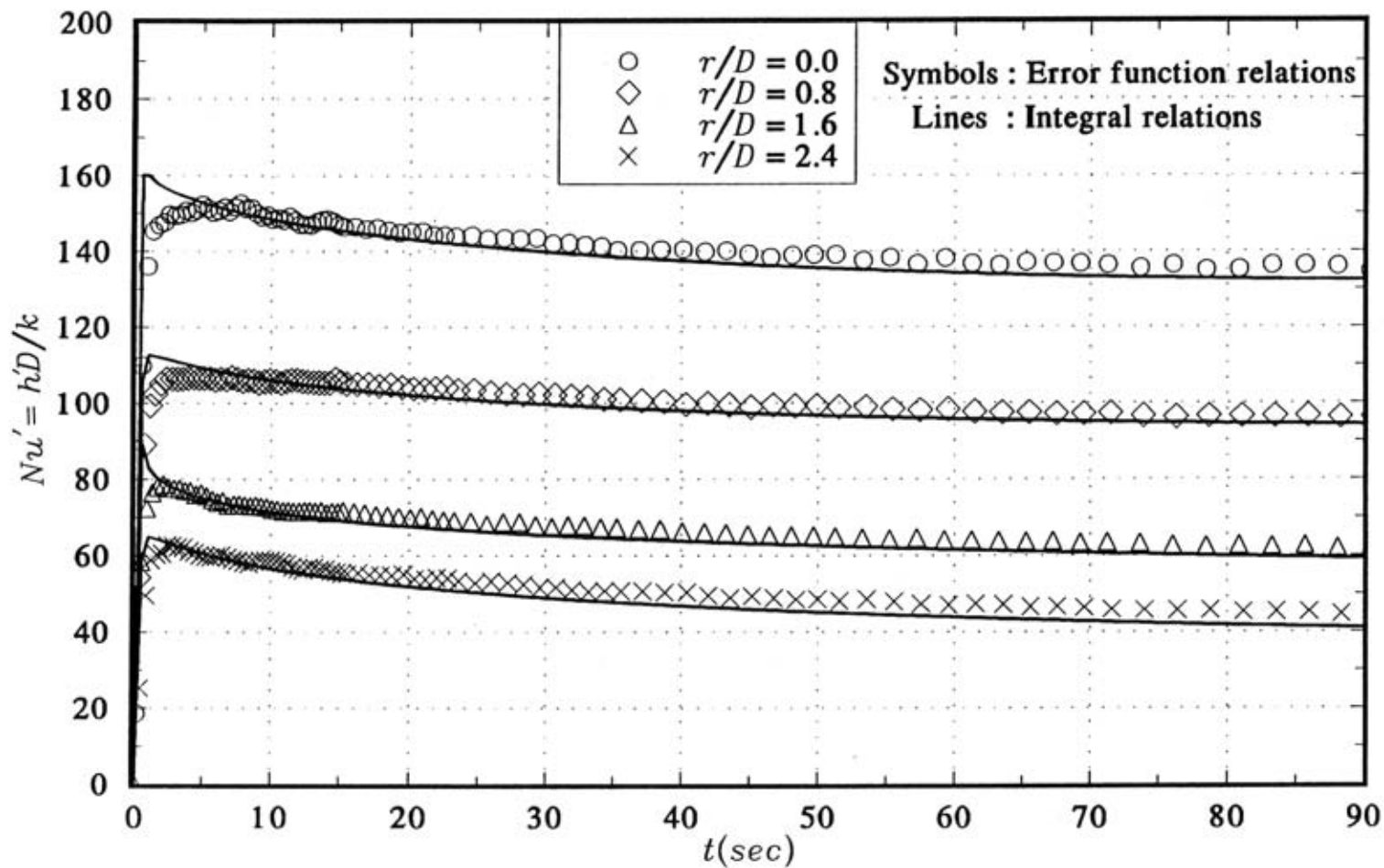
Figure 3.21 Nusselt number variations in time obtained from the temperature histories at 4 separate radial locations.
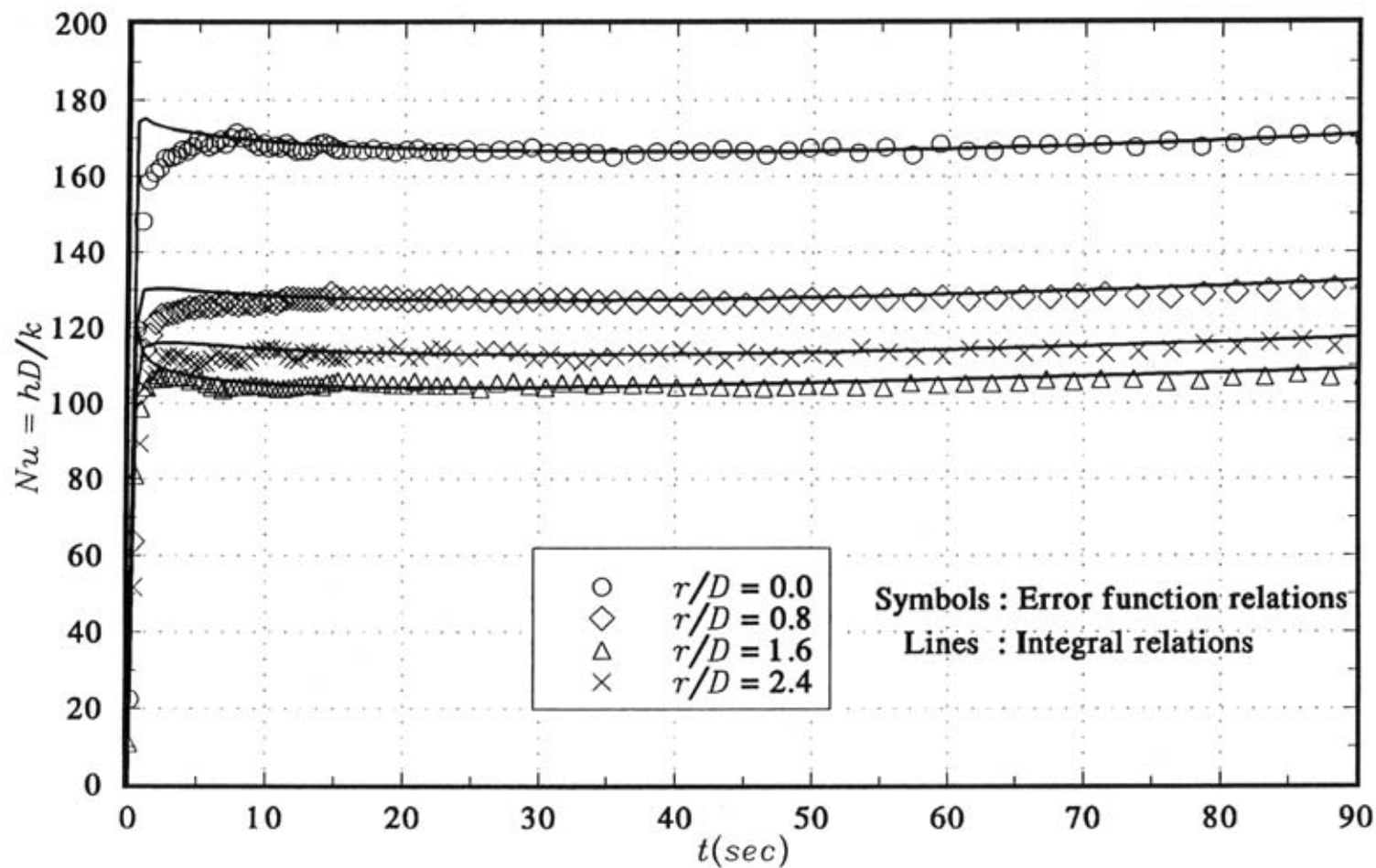
Figure 3.22 Nusselt number variations in time obtained from the temperature histories
at 4 separate radial locations.
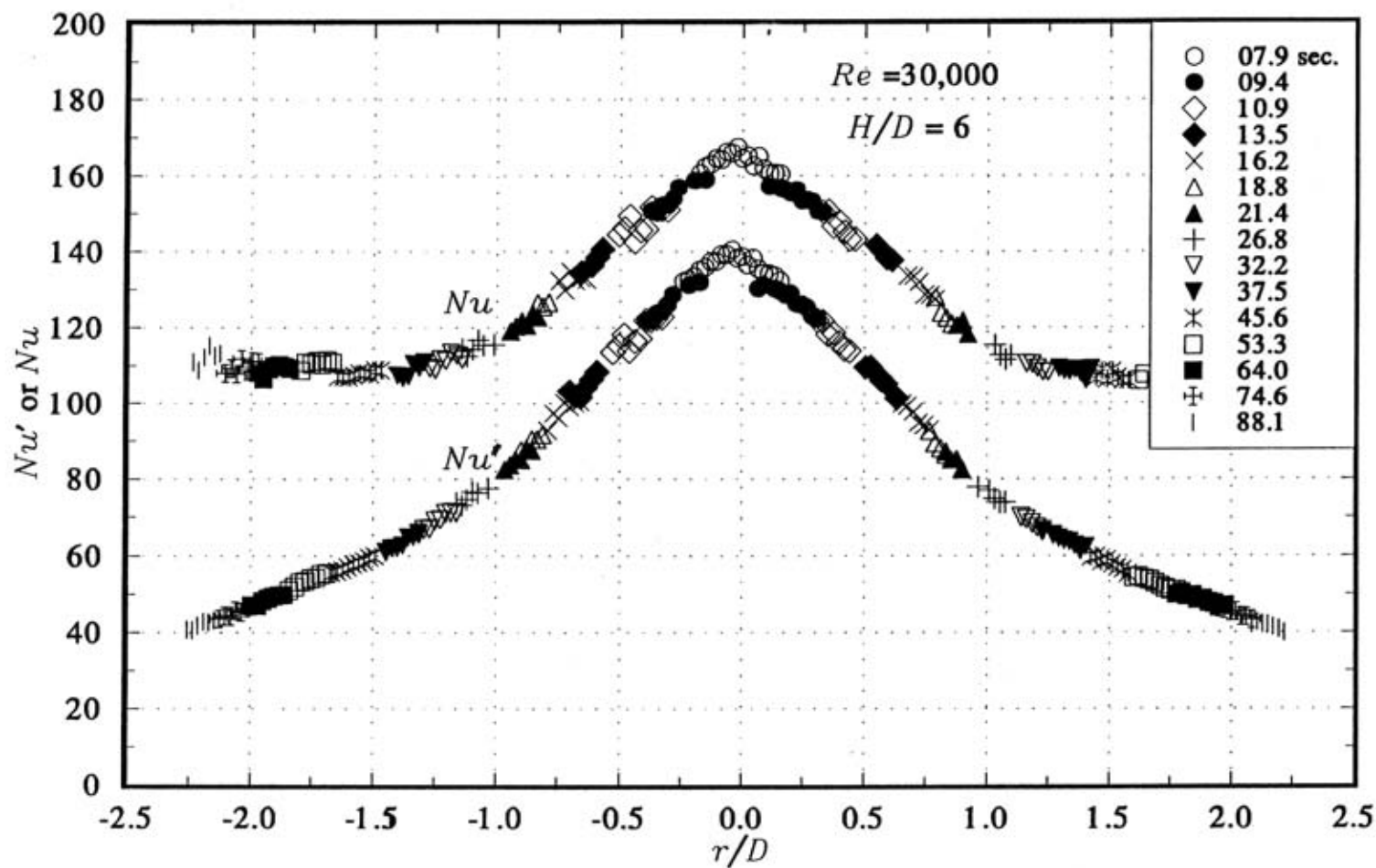
Figure 3.23 Nusselt number distributions obtained using 15 discrete color images sampled at different times.
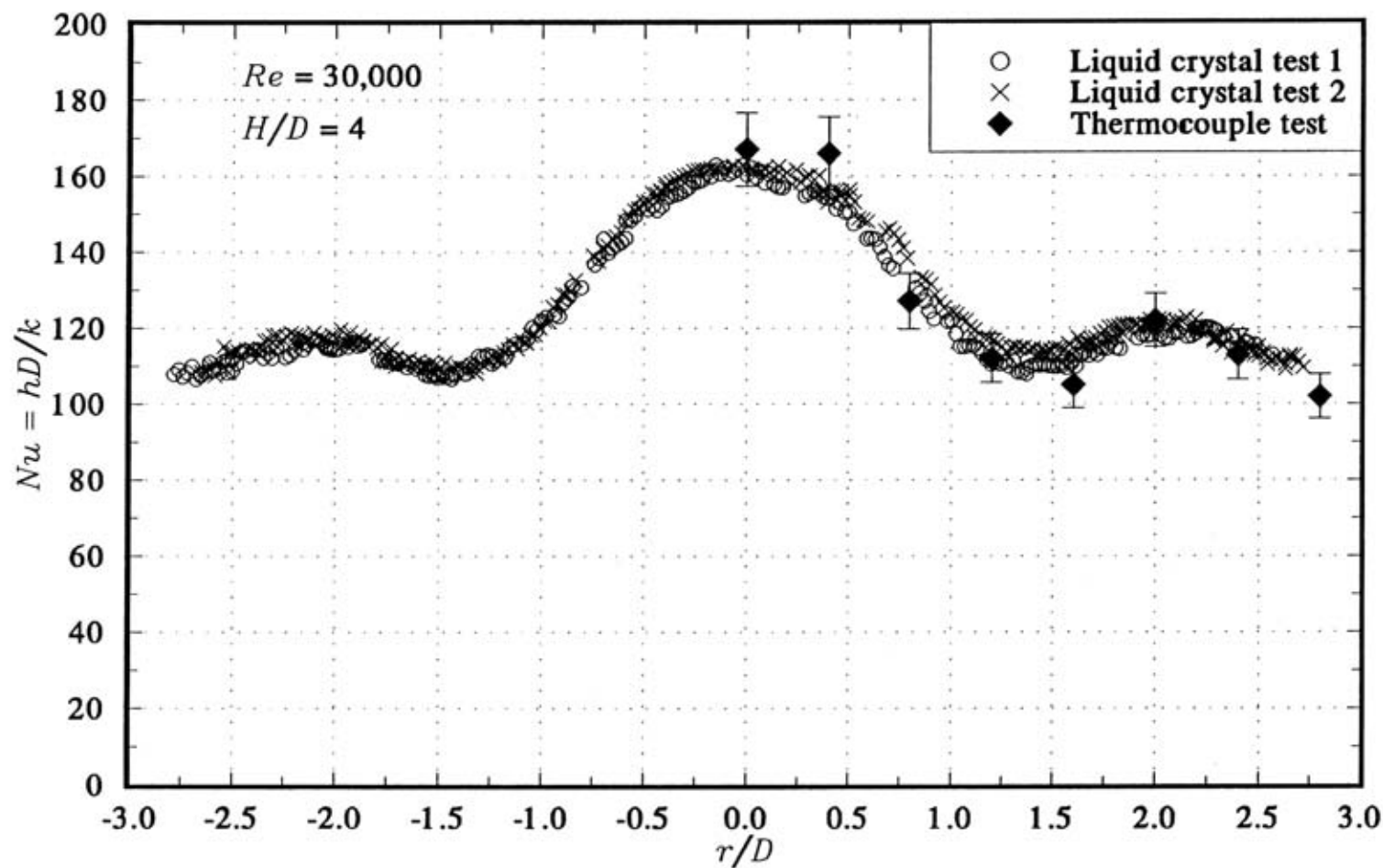
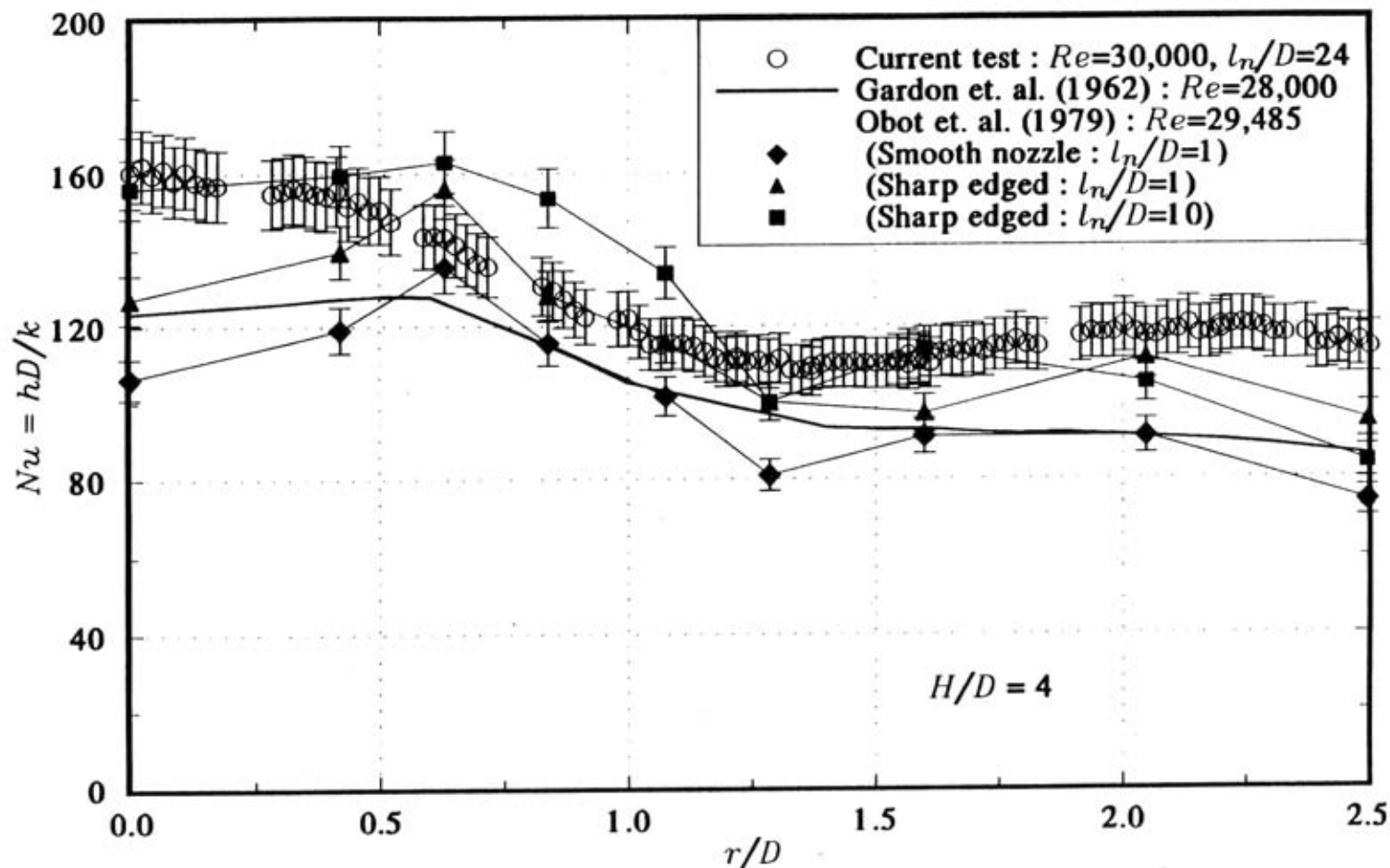Figure 3.24 Comparison of the Nusselt numbers measured using thermocouples and the hue capturing technique.

Figure 3.25 Comparison of the current Nusselt number results with
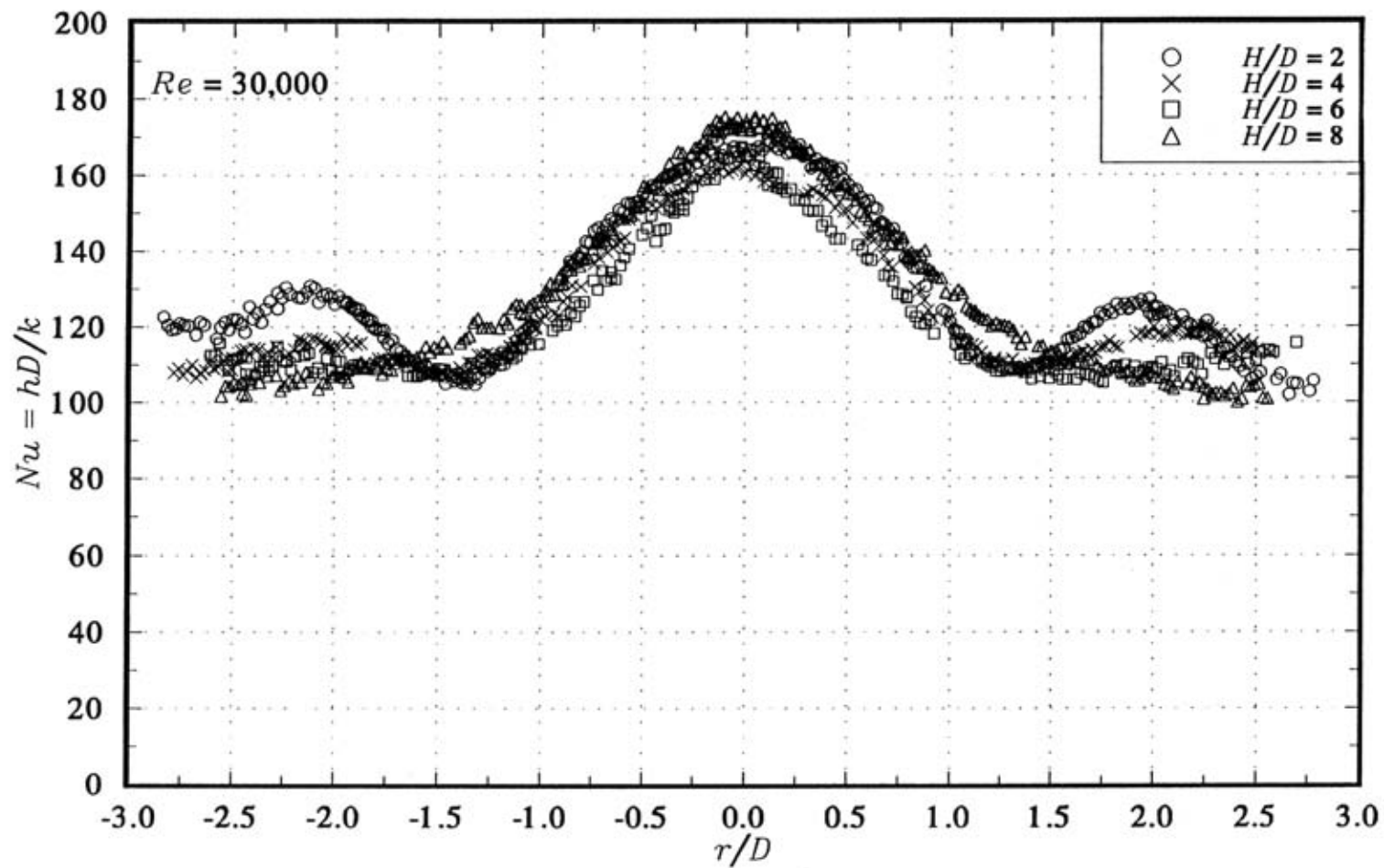other studies investigated with conventional tools.

40

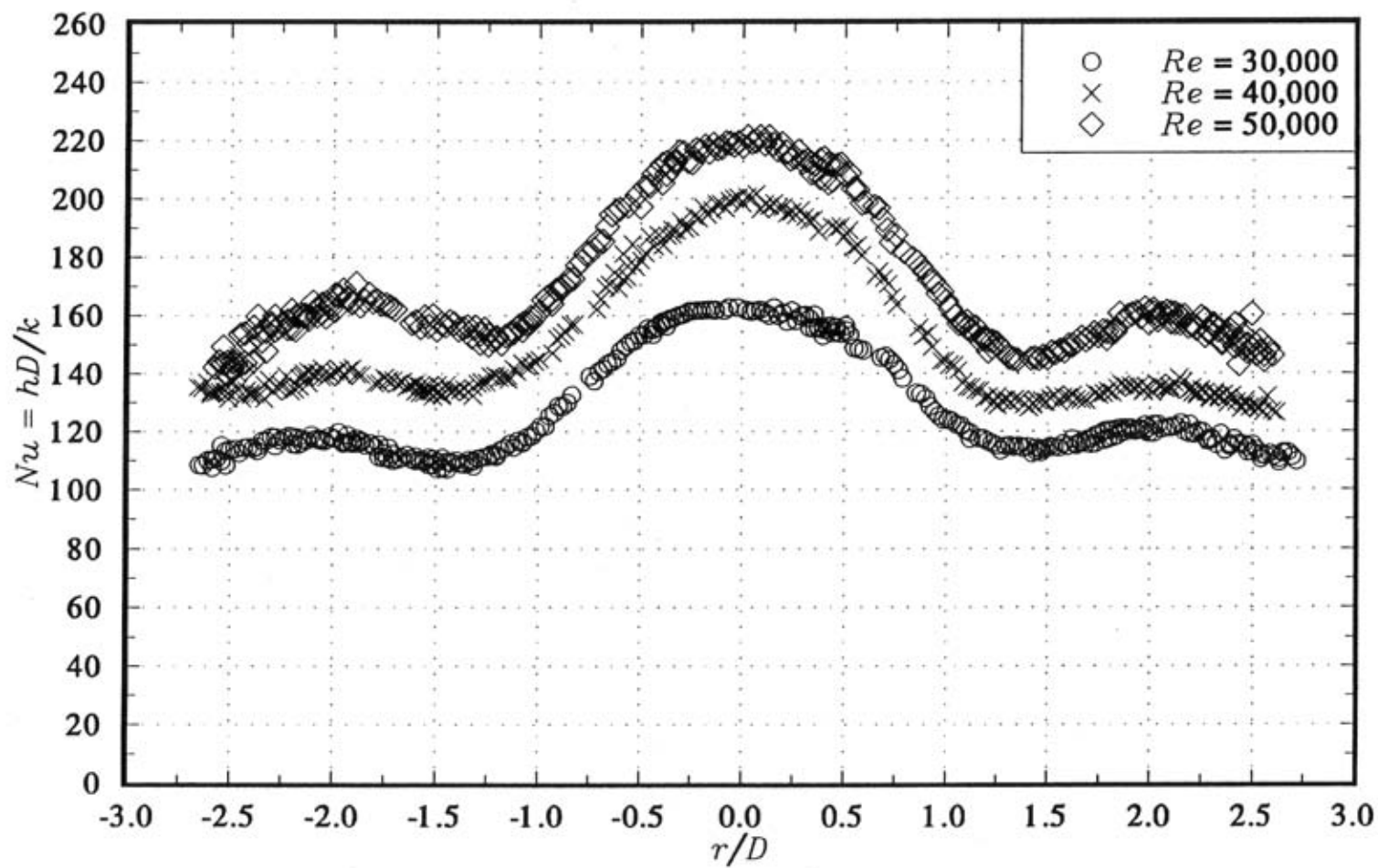Figure 3.26 The effect of the nozzle-to-plate distance on Nusselt number distributions, $Re = 30,000$.

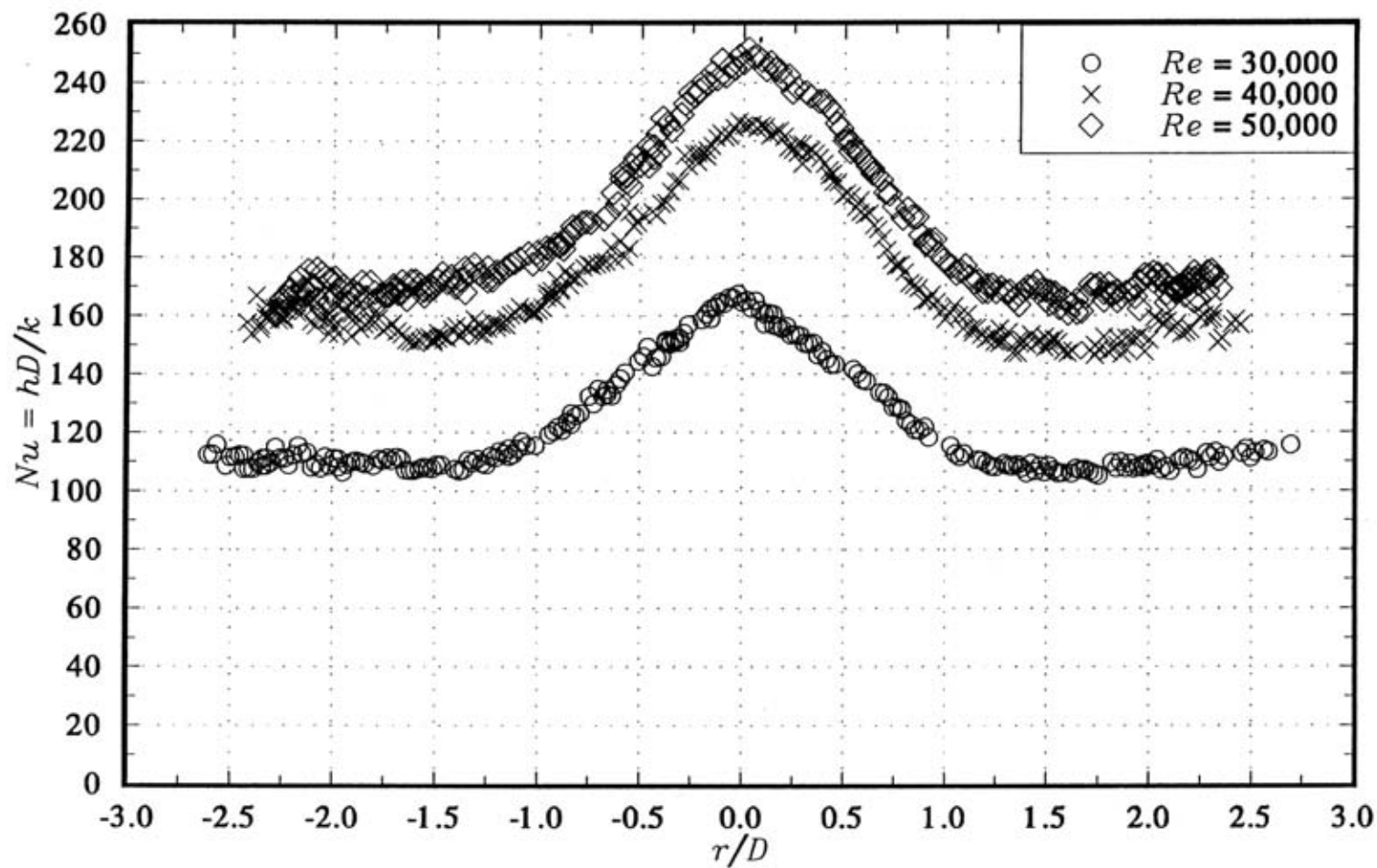Figure 3.27 Reynolds number effect on Nusselt number distributions, $H/D = 4$.

Figure 3.28 Reynolds number effect on Nusselt number distributions, $H/D = 6$.